NASA Technical Memorandum 84902

FLIGHT AND WIND-TUNNEL CORRELATION OF BOUNDARY-LAYER TRANSITION ON THE AEDC TRANSITION CONE

David F. Fisher and N. Sam Dougherty, Jr.

November 1982

NASA

NASA Technical Memorandum 84902

FLIGHT AND WIND-TUNNEL CORRELATION OF BOUNDARY-LAYER TRANSITION ON THE AEDC TRANSITION CONE

David F. Fisher
Ames Research Center
Dryden Flight Research Facility
Edwards, California

and

N. Sam Dougherty, Jr.
Rockwell International
Huntsville, Alabama

National Aeronautics and
Space Administration

1982

FLIGHT AND WIND-TUNNEL CORRELATION OF BOUNDARY-LAYER TRANSITION ON THE AEDC TRANSITION CONE

David F. Fisher
NASA Ames Research Center
Dryden Flight Research Facility
Edwards, California 93523
U.S.A.

N. Sam Dougherty, Jr.*
Rockwell International
Huntsville, Alabama 35801
U.S.A.

SUMMARY

Transition and fluctuating surface-pressure data were acquired on a 10° included angle cone, using the same instrumentation and technique over a wide range of Mach and Reynolds numbers in 23 wind tunnels and in flight. Transition was detected with a traversing pitot-pressure probe in contact with the surface. The surface-pressure fluctuations were measured with microphones set flush in the cone surface. Good correlation of end-of-transition Reynolds number Re_T was obtained between data from the lower-disturbance wind tunnels and flight up to a boundary-layer edge Mach number, $M_e = 1.2$. Above $M_e = 1.2$, however, this correlation deteriorates, with the flight Re_T being 25 to 30% higher than the wind tunnel Re_T at $M_e = 1.6$. The end-of-transition Reynolds number correlated within ±20% with the surface-pressure fluctuations, according to the equation

$$Re_T = 3.7 \times 10^6 \left[\left(\frac{\sqrt{\overline{p'_s}^2}}{q_\infty} \right) 100 \right]^{-0.25}$$

Broad peaks in the power spectral density distributions indicated that Tollmien-Schlichting waves were the probable cause of transition in flight and in some of the wind tunnels.

NOMENCLATURE

F	nondimensional peak center frequency, $(2\pi f \nu_e)/U_e^2$
f	frequency, Hz
$G_x(f)$	power spectral density function
H	1962 standard atmosphere pressure altitude, m (ft)
L	length of cone with extension, 113.0 cm (44.5 in)
M	Mach number
p	pressure, N/m^2 (lb/ft^2)
p'	fluctuating pressure, N/m^2 (lb/ft^2)
$\sqrt{\overline{p'_s}^2}$	average static root-mean-square fluctuating pressure, N/m^2 (lb/ft^2)
q	dynamic pressure, N/m^2 (lb/ft^2)
Re_T	end-of-transition Reynolds number
Re_T'	end-of-transition Reynolds number not corrected to adiabatic temperature
Re_t	onset-of-transition Reynolds number
Re_x	Reynolds number based on length from cone apex
T	temperature, K (°R)
U	velocity, m/sec (ft/sec)
U/ν	unit Reynolds number, per m (per ft)
X_T	end-of-transition location, cm (in)
X_t	onset-of-transition location, cm (in)
x	distance along a cone ray from the cone ℓ x, cm (in)
α	cone angle of attack with respect to airstream, deg
β	cone sideslip angle with respect to airstream, deg
ν	kinematic viscosity, m^2/sec (ft^2/sec)
φ	cone azimuthal angle relative to cone top center ray (Fig. 1(b)), deg

Subscripts:

aw	adiabatic wall
e	boundary-layer edge
max	maximum
p	traversing pitot
t	total
w	at wall

*Formerly with ARO, Inc., Arnold Air Force Station, Tennessee 37389, U.S.A.

α	in pitch plane	2	at aft microphone on cone surface (x = 66.0 cm (26 in))
β	in sideslip plane	∞	free stream
1	at forward microphone on cone surface (x = 45.7 cm (18 in))		

1.0 INTRODUCTION

The importance of Reynolds number in scaling aerodynamic-model test results from wind tunnels to full-scale flight vehicles is well known, and the data from the small models have to be suitably adjusted for Reynolds number effects. Because these adjustments are usually based on simple extrapolations or ratios of Reynolds number, they introduce some errors. The viscous effects on the boundary-layer growth on a body are cumulative and can create boundary-layer/shock interactions or separations at transonic and supersonic speeds that differ significantly with the scale-up from model to full-scale vehicles. The location at which the boundary layer changes from laminar to turbulent flow influences boundary-layer growth and has a significant effect on these interactions and separations. Hence, the transition Reynolds number based on the point of transition and on the unit Reynolds number is a key parameter in the overall similitude of flow.

As pointed out by Potter and Whitfield (Ref. 1), one cannot expect a constant value of transition Reynolds number relative to a characteristic length Reynolds number when scaling transition-sensitive data. As noted by Morkovin (Ref. 2), there are no clear-cut rules to ensure that the transition locations predicted for general body shapes will be accurate. A common practice in wind-tunnel testing is to force transition with artificial trip devices, particularly when there is a large mismatch in model and full-scale Reynolds numbers. The fixing of transition provides a gross approximation of the flow, even though the discrete characteristics of the boundary layer on the model may not be the same as on the full-scale vehicle. The usual correction is to subtract out the skin friction of the model, using a flat-plate friction law for the wind-tunnel Reynolds number, then adding back the skin friction for the full-scale vehicle at flight Reynolds numbers.

Treon et al. (Ref. 3) have shown, however, significant differences in data for the identical model, Mach numbers, and Reynolds numbers in three different wind tunnels because of flow quality. In addition, Mabey (Ref. 4) has also shown that flow unsteadiness can affect both static and dynamic test results. Three pertinent factors are involved in wind-tunnel flow quality: uniformity of free-stream velocity, uniformity of streamlines or flow angle, and free-stream disturbance level.

During the past decade, a comprehensive series of tests in the United States and western Europe have been performed to investigate the effects of free-stream disturbances on boundary-layer transition and Reynolds number scaling. In a cooperative effort by the U.S. Air Force, National Aeronautics and Space Administration, U.S. Navy, the Calspan Corp., and the governments of the United Kingdom, France, and the Netherlands, the flow disturbance levels of 23 wind tunnels (Table 1) and in flight have been documented. A sharp, slender, smooth cone, known as the Arnold Engineering Development Center (AEDC) 10° Transition Cone, was used. Throughout the program, care was exercised to maintain the model in the same unblemished condition. The results obtained testify to the diligence exercised by the many test personnel who participated in this investigation. The flight-test program was performed by the Dryden Flight Research Facility, Edwards, California. The results of the test program were enhanced because the experiments could be repeated—sometimes as long as 8 years later—in wind tunnels (at AEDC and Ames Research Center) whose configurations were unchanged. Likewise, selected flight-test points were repeated weeks apart.

The tests reported here were conducted under the scrutiny and beneficial guidance of the U.S. Transition Study Group, Prof. Eli Reshotko, Chairman. To a great extent, the credibility of the results is attributable to the critiques, advice, and guidance sought and received on a continuous basis from this group since 1974.

The wind-tunnel data from this investigation were published by the individuals and organizations involved in Refs. 5 to 10 and are summarized in Ref. 11. The flight data were reported in Ref. 12. The correlations between wind-tunnel data and flight data were reported in Refs. 13 and 14. Many of these data were used in an independent review reported in Ref. 15.

2.0 APPROACH

Transition and pressure fluctuation data were acquired using a simple conical body and instrumentation over a wide range of Reynolds and Mach numbers at zero incidence and adiabatic wall conditions in a number of wind tunnels and in flight. The body shape chosen was the AEDC Transition Cone, a sharp, slender cone with a semi-apex angle of 5°. With the exception of the flow over a flat plate, the flow over a slender cone at zero incidence is the simplest known. At subsonic speeds, the flow experiences only a small axial favorable pressure gradient and virtually a zero pressure gradient at supersonic speeds after shock attachment. In addition, the cone does not have the end effects of a flat plate that result from the finite span of the plate, it is relatively easier to manufacture, and, because it does not generate much lift at low incidence, it is better suited to flight test.

The same instrumentation and techniques were used to detect the onset and the end of transition and to document the pressure fluctuations in the wind tunnels and in flight. A traversing pitot-pressure probe in contact with the surface was used to detect the onset and end of transition. The pressure fluctuations at the cone surface were measured with microphones set flush in the cone. The microphone-measured results approximate those of free-stream conditions only when the boundary layer is laminar.

3.0 TEST APPARATUS

The AEDC 10° Transition Cone (Fig. 1) was used for all transition and surface-pressure fluctuation measurements. The cone had a semivertex angle of 5° and an apex bluntness less than 0.10 mm (0.004 in) in equivalent diameter. The cone was made of stainless steel, highly polished, with a surface finish of 0.25 μm (10 μin) or better. It was 91.4 cm (36.00 in) long, with a cone extension that extended the length to 113.0 cm (44.50 in).

Transition was detected along the 0° ray (Fig. 1), using a traversing pitot-pressure probe (Fig. 2) in contact with the surface. A 0.238-cm- (0.094-in-) diameter semiconductor strain-gage transducer was close-coupled and mounted inside the probe.

The surface-pressure fluctuations were measured, using two flush-mounted microphones at distances of 45.7 cm (18.0 in) and 66.0 cm (26.0 in) aft of the cone apex and at azimuthal angles of φ = 225° and 180°, respectively (Figs. 1 and 3). Condenser microphones, 0.635 cm (0.25 in) in diameter, were used for most of the wind-tunnel tests and for the low-speed portion of the flight test. For the high-speed portion of the flight tests, 0.238-cm- (0.094-in-) diameter semiconductor strain-gage-type microphones were used because of the higher recovery temperatures that were reached. Overlapping data from the two types of microphones confirmed that there was no appreciable difference in response over a bandwidth from 200 Hz to 20 kHz for the flight tests. Some corrections to the condenser microphone data at frequencies above 40 kHz were required in the wind tunnel at low ambient pressure. For the flight test only, a semiconductor strain-gage-type microphone, mounted on the knee of the traversing mechanism, measured the pressure fluctuations in the free stream, as shown in Fig. 4.

The cone temperature was determined from an iron-constantan thermocouple epoxied in a small hole on the lower centerline ray at x/L = 0.80. When transition was measured on the cone, the thermocouple would be in a turbulent boundary layer and a turbulent recovery factor would be applicable.

For the flight tests and for some wind-tunnel tests, a hemispherical head-sensing probe (Fig. 1) was mounted below and behind the cone apex to measure airspeed, free-stream static pressure, and flow incidence. A ring of orifices, 4.7 probe diameters aft of the probe tip, were used to determine free-stream static pressure. The free-stream static pressure was combined with the impact pressure from the orifice at the stagnation point to calculate Mach number. Two pairs of orifices in the pitch and yaw planes, 40° from the stagnation point, were used to determine angle of attack and angle of sideslip, respectively.

4.0 PROCEDURE

4.1 Flight Test

For the flight tests, the cone was mounted on the noseboom of an F-15 aircraft (Fig. 5). In order to obtain results that could be correlated, the flight and wind-tunnel data had to be obtained at flow conditions as nearly identical as possible. This required that the pilot fly the airplane at a constant airspeed and altitude, keeping the cone at zero incidence and at adiabatic conditions. An in-flight calibration of the hemispherical head-sensing probe for airspeed and altitude was made, using the pacer method (Ref. 16) at subsonic speeds and radar tracking (Refs. 17 and 18) at subsonic and supersonic speeds. The probe was calibrated for angle of attack and angle of sideslip in several wind tunnels. Both the airspeed and incidence calibrations are given in Ref. 12. The inclination of the cone sting with respect to the aircraft centerline was preset before flight to compensate for the expected aircraft trim angle of attack. Aim test-point conditions (Mach number, altitude, and trim angle of attack) were specified, and the pilot adjusted the airspeed to center the cone angle-of-attack indicator to zero.

The cone angle of sideslip was zeroed, using the rudders. Upper atmospheric temperature data from early morning radiosonde balloons were used to calculate the aim cone adiabatic wall conditions. For Mach numbers of 1.2 and above, the cone had to be preconditioned on the ground with a hot-air heater (Fig. 6). The cone was heated for about 1 hr, to a temperature of 105° C to 115° C (220° F to 240° F). The heater was removed just before takeoff, and the aircraft climb schedule was adjusted so that the cone would be at the predetermined adiabatic-wall temperature when the aircraft reached the aim test conditions. Data from the aircraft and cone were monitored continuously in real time on strip charts and video displays, and the information was relayed to the pilot. For the lower Mach numbers, it was sometimes necessary to cool the cone. This was done by flying the aircraft at a higher altitude and lower temperature than the test point until the desired cone adiabatic-wall temperature was reached.

A history of the free-stream conditions during a typical pitot-probe traverse is shown in Fig. 7. As can be seen, the conditions were quite stable, with angle of attack and angle of sideslip within ±0.2°. A pitot-probe traverse during the same test conditions is shown in Fig. 8. The onset of transition X_t was defined, as it was for the wind-tunnel data, as the location at which the minimum pitot pressure occurred. Likewise, the end of transition X_T was defined as the location at which the maximum pitot pressure occurred. Both these locations are shown in Fig. 8.

The flight-test matrix is shown in Fig. 9. The flight data are grouped by the different aircraft trim angles that were flown and correspond to nominal dynamic pressures. Test points at the same trim angle correspond approximately to the curves of constant unit Reynolds number, U/ν. Also shown in Fig. 9 is the equivalent combined envelope for the wind-tunnel data of this study. As can be seen, the flight data encompass most of the wind-tunnel test data, up to a Mach number of 2.0.

4.2 Wind Tunnel Tests

Every procedural consideration described for the flight test was present in the wind-tunnel tests, except that the problems associated with obtaining test conditions were much simpler. The cone had to be at zero incidence and adiabatic-wall temperature. No thermal preconditioning was necessary, for the temperature excursions were not nearly so severe, and there was ample time to wait for the cone to reach thermal equilibrium with the flow. Some wait between data points was necessary for T_w/T_{aw} to approach 1.0, following a large Mach number

change. Usually, the sequence of test points could be planned to progress through small incremental changes in Mach number. Most wind tunnels could hold total temperature constant within ±3° C (±5° F) on a given test point. The best sequencing of points was to change U_∞/ν_∞ at constant M_∞ in a variable-density tunnel by changing p_t at constant T_t. In atmospheric tunnels, one can only change M_∞.

A bigger problem in the wind tunnels was defining the incidence angle. In some cases, negligible flow angularity was assumed and the cone was simply aligned carefully to the test section centerline. In other cases, flow angularity was known or suspected and a set of aerodynamic centering calibrations was performed at each Mach number, using the transition variation with incidence angle when the pitot probe trace was 90° relative to the windward stagnation ray. This was accomplished using the model pitch, yaw, and roll capabilities of a given wind tunnel to define vertical and horizontal components of the stream angle. The largest stream angle found was 1.5°.

In general, data were acquired for a matrix of Mach numbers and Reynolds numbers covering the full operating envelope of a given wind tunnel. The normal test-section ventilation procedures were followed for each transonic tunnel near $M_\infty = 1.0$. The minimum transonic wind-tunnel test section size was 4 by 4 ft, so wall interference attributable to transonic blockage phenomena was not considered to be a significant problem. Long sting-support systems were used in transonic tunnels to minimize support-system blockage and radiated aerodynamic noise influence. The sting-supported cone vibrations were generally at frequencies less than abou. 10 Hz and of amplitudes small enough that no coherent oscillations could be found in the pitot pressure that could be identified as vibratory-motion related.

Measurements of relative humidity in wind tunnels are not usually reliable. The criterion generally used for acquiring data in these experiments was not to proceed if there was visible fogging. However, in some cases when dew points were above about -23° C (-10° F) at $M_\infty \geq 1.8$, indicated by available instrumentation, precautions were taken to verify that the indicated M_∞ and U_∞/ν_∞ were within the wind-tunnel calibration.

5.0 RESULTS

5.1 Laminar Instability

Indications of laminar instabilities in the boundary layer were found in the microphone power spectral density distributions during the flight test. For purposes of illustration, the spectra obtained at two test points from all three microphone signals (free-stream impact, forward-cone, and aft-cone) are shown in Fig. 10. In Fig. 10(a), the forward-cone microphone was under transitional flow and the aft-cone microphone was under fully developed turbulent flow. In fig. 10(b), the forward-cone microphone was under laminar flow and the aft-cone microphone was under transitional flow. In all cases when the boundary layer was laminar or transitional, there was a broad peak in the pressure-fluctuation spectra, similar to those shown in Fig. 10. The nondimensional frequency at which the peak occurs is denoted by F in Fig. 10; the subscripts 1 and 2 refer to the forward- and aft-cone microphones, respectively.

Power spectral densities recorded from several flights at the same nominal Mach numbers but at different Reynolds numbers are shown in Fig. 11(a) and (b). The dominant feature in these cone boundary-layer spectra is the peak, which decreases in frequency and increases in power as Re_x increases at a given M_e. Finally, at the location near the end of transition, X_T, the peak disappears into the smooth, broadband spectrum characteristic of a turbulent boundary layer.

The spectral peaks appeared to exhibit a prescribed behavior in terms of the variation of absolute frequency f with M_e, as shown in Fig. 12 for a dynamic pressure of 14.4 kN/m^2 (300 lb/ft^2). The peak center-frequencies increase as M_e increases. A ratio of the frequencies f_1/f_2, when peaks occurred in the spectra from both microphones at a given flight condition, was approximately the inverse of the ratio of the distance from the cone apex, $(x_2/L)/(x_1/L)$, and therefore the inverse of the microphone Reynolds number, Re_{x_2}/Re_{x_1}. Hence, the peak frequencies are functions of both Re_x and M_e.

The nondimensional peak center-frequencies are shown in Fig. 13, plotted as a function of $(Re_x)^{0.50}$; they show a clear dependence on Reynolds number and Mach number. The data agree well with recent calculations by Mack, since his publication of Ref. 19 adjusted by the usual cone-planar similarity rule (where the Reynolds number on a cone is 3 times that on a flat plate). The calculations by Mack are for the first-mode laminar instability, that is, Tollmien-Schlichting waves, and the calculations agree with the characteristics of the spectra; thus, Tollmien-Schlichting waves are probably the cause of transition.

A reexamination of the wind-tunnel power spectral distributions after the flight test revealed indications of Tollmien-Schlichting instabilities in two Langley wind tunnels, the 4- by 4-ft supersonic pressure tunnel and the Unitary Plan Wind Tunnel, where the pressure fluctuation levels, $\sqrt{\overline{p_s'^2}}/q_\infty$, were the lowest measured. Microphone spectra for the 4- by 4-ft supersonic pressure tunnel at Langley Research Center for a Mach number of 1.61 are shown in Fig. 14. These data are either for a laminar or transitional boundary layer. Broad peaks in the spectra, similar to those observed in flight, are evident for the forward microphone at $Re_{x_1} = 4.41 \times 10^6$ and at $Re_{x_2} = 4.26 \times 10^6$ for the aft microphone.

5.2 Flight Transition Reynolds Number

In preparation for the flight tests, the effect of incidence on transition location was determined in various NASA wind tunnels (Fig. 15). Note that at small negative angles of attack, with the surface pitot probe on the windward ray, the effect is small for Mach numbers between 0.6 and 2.2. The effect of sideslip can be significant at angles greater than 0.25°.

During the flight tests, it was possible to control the temperature of the transition cone within ±6% of the adiabatic-wall temperature, T_{aw}, for about 90% of the test points, using the techniques described in Sec. 4.1 (Flight Test). Even this small deviation in temperature had a large influence on transition location, however, as shown in Fig. 16. The data have been grouped by Mach number and nondimensionalized by the transition Reynolds number corrected to adiabatic-wall temperature determined from fairings of the flight data for each nominal Mach number. The sensitivity of transition Reynolds number to heat transfer appears to have been essentially independent of Mach number and proportional to the temperature ratio T_w/T_{aw}. The trend of the data in Fig. 16 shows a strong heat-transfer influence on transition, delayed transition occurring when the boundary layer was cooled ($T_w/T_{aw} < 1.0$), earlier transition occurring when the boundary layer was heated ($T_w/T_{aw} > 1.0$). Also shown in Fig. 16 are data obtained during a rapid excursion of total temperature at $M = 1.2$ in the 4-ft transonic (4T) wind tunnel at AEDC. These wind tunnel results show the same trend as the flight data. According to the theoretical flat-plate e^9 method from Ref. 20, the onset of transition at a Mach number of 0.85 also follows the trend of the flight data. A curve was fitted through the flight data and used for correcting nonadiabatic data to adiabatic conditions.

The end-of-transition Reynolds numbers measured in flight, corrected to adiabatic-wall temperatures, are shown as functions of local Mach number in Fig. 17. This figure includes 82 test points (39 of which were acquired at supersonic speeds) gathered from 27 flights over 2 1/2 months. The data form a nearly linear band for both the end-of-transition and the onset-of-transition Reynolds numbers. Both were strong functions of Mach number. End-of-transition Reynolds numbers ranged from about 3.5×10^6 at a Mach number of 0.5 to above 9.0×10^6 at Mach numbers above 1.6. Actual measurements of X_t, X_T, and the corresponding flight conditions are tabulated in Ref. 12, together with the corrected values of end-of-transition Reynolds number Re_T, and onset-of-transition Reynolds number Re_t. Figure 18 shows that the ratio of onset-of-transition Reynolds number to end-of-transition Reynolds number is independent of Mach number and dynamic pressure and has a mean value of 0.86. Most of the data are within ±5% of this mean value.

Transition Reynolds number was plotted as a function of unit Reynolds number in Fig. 19 for nominal Mach numbers to determine whether the present data had the unit Reynolds number effect shown for higher Mach numbers in Refs. 11, 21, and 22. Even at Mach numbers at which there were substantial data over a wide range of unit Reynolds numbers at adiabatic conditions, the data are inconclusive.

5.3 Flight Disturbance Environment

Naturally growing Tollmien-Schlichting waves can be detected only in a low-disturbance, free-stream environment. As shown by the overall pressure fluctuations from the free-stream impact microphone (Fig. 20), the level of pressure fluctuations in the flight environment was very low. The pressure fluctuations in flight varied from about 0.16% at the lower Mach numbers to 0.017% near Mach 2, when normalized by the free-stream dynamic pressure q_∞. The different flags on the symbols, which denote flights made on different days, indicate the day-to-day variations in the atmosphere. The pressure fluctuations do not seem to be dominated by engine noise, although some discrete tones appeared randomly in the spectra, some of which may have come from the engine inlets, fans, or compressors.

The cone surface static-pressure fluctuations in the boundary layer were sensed by the surface microphones set flush in the cone. When the cone boundary layer was turbulent, the cone-surface microphones recorded pressure fluctuations in the near-field turbulent boundary layer. When the boundary layer was transitional, the amplification of the low end of the frequency spectrum during transition produced large overall values of indicated pressure fluctuation. Only under laminar conditions could the cone-surface microphones measure pressure fluctuations imposed from the free stream, and those measurements were altered by the laminar boundary-layer receptivity. As the spectral data in Figs. 10 and 11 show, the laminar boundary layer selectively amplifies certain frequencies in the spectrum, increasing some of the values sensed by the microphone.

The cone-surface static-pressure fluctuations in the laminar boundary layer $\sqrt{\overline{p_s'^2}}$ are shown normalized by q_∞ in Fig. 21 as a function of M_e. As shown, the laminar pressure fluctuations decrease with increasing M_e. A comparison of Figs. 20 and 21 shows that at the highest M_e the cone-surface pressure fluctuation is essentially the same as the free-stream impact-pressure fluctuation. The differences between the cone-surface and free-stream impact-pressure fluctuation amplitudes increase as M_e decreases. As before, the different flags on the symbols (Fig. 20) denote flights on different days to indicate day-to-day variations. The open symbols denote data acquired with the semiconductor strain-gage-type microphones used at the higher Mach numbers and higher temperatures. The solid symbols denote data acquired with condenser microphones like those used in most of the wind tunnels. The data from both types of microphones agree well. The laminar and transitional spectra measured by both sets of microphones had the same characteristics, verifying that the peaks were associated with the boundary layer and that they were not anomalies introduced by the sensors.

5.4 Correlation of Wind Tunnel and Flight Data

The wind tunnels used in these experiments were classified into four groups, based on their distinguishing geometry:

Group 1: Slotted or solid-wall transonic and subsonic tunnels
Group 2: Perforated-wall transonic tunnels
Group 3: Two-dimensional-nozzle supersonic tunnels
Group 4: Sliding-block-nozzle supersonic tunnels

The pressure fluctuation levels measured under the laminar boundary layer on the cone from the wind tunnels are shown in Fig. 22. Also shown is an envelope for the flight pressure fluctuation data from Fig. 21. The dashed curve in Fig. 22 is a relationship from Lowson (Ref. 23) for estimating the pressure fluctuations at the wall beneath an attached turbulent boundary layer. The microphones on the cone sense pressure fluctuations from all sources, including the wind-tunnel walls. As shown in Fig. 22(a), essentially all the data from the lower disturbance tunnels (groups 1, 3, and 4) are below this curve. However, the flow disturbance measured in the lower disturbance tunnels was about twice that measured in flight. For the higher disturbance tunnels (group 2, Fig. 22(b)), the flow disturbance is greater than Lowson's curve and approximately an order of magnitude greater than the flight data.

The end-of-transition Reynolds number Re_T is presented in Fig. 23 for the group 1, 3, and 4 wind tunnels. The wind-tunnel data have been extrapolated for nominal unit Reynolds numbers of 6.6×10^6/m (2.0×10^6/ft), 9.8×10^6/m (3.0×10^6/ft), and 13.1×10^6/m (4.0×10^6/ft). There is a 14% increase in Re_T for unit Reynolds numbers between 6.6×10^6/m (2.0×10^6/ft) and 13.1×10^6/m (4.0×10^6/ft) at supersonic speeds in the wind tunnels. The end-of-transition Reynolds numbers from the lower disturbance tunnels (groups 1, 3, and 4) agree well with the flight data up to $M_e = 1.2$. Above $M_e = 1.2$, the correlation deteriorates, and at $M_e = 1.6$ the flight Re_T is 25% to 30% higher than the wind-tunnel Re_T. For the higher disturbance tunnels (group 2), shown in Fig. 24, there is a very poor correlation between wind-tunnel and flight end-of-transition Reynolds numbers.

The onset-of-transition Reynolds numbers from the lower disturbance wind tunnels is shown in Fig. 25. The flight data from Fig. 17(b) are shown by the envelope. At subsonic speeds, the data from the Naval Ship Research and Development Center (NSRDC) tunnel showed good correlation with the flight data. The onset-of-transition Reynolds numbers from the Langley 16-ft transonic dynamics tunnel (NASA/Langley 16 TDT) were lower than those of most of the flight data. Unfortunately, onset of transition from the several other lower disturbance tunnels at transonic speed was either poorly defined by the surface pitot-pressure-probe technique or lost because of poor pitot-probe contact with the cone surface.

The ratio of onset-of-transition Reynolds number to end-of-transition Reynolds numbers is shown in Fig. 26 for the wind tunnels. The flight data are represented by the fairings. The wind-tunnel ratios of onset-of-transition to end-of-transition Reynolds numbers are less than those in flight at unit Reynolds numbers of 6.6×10^6/m (2.0×10^6/ft) and 9.8×10^6/m (3.0×10^6/ft) between Mach numbers of 0.5 to 2.0. At a unit Reynolds number of 13.1×10^6/m (4.0×10^6/ft) the correlation between flight and wind tunnel data is much better. This unit Reynolds number effect was not observed in flight, even though it covered approximately the same Reynolds number range.

The end-of-transition Reynolds number as a function of the flow disturbance levels from wind tunnel and flight data are presented in Fig. 27. This figure includes data from all Mach numbers and unit Reynolds numbers. The end-of-transition Reynolds number correlated within ±20% with the surface fluctuating root-mean-square pressure level according to the equation

$$Re_T = 3.7 \times 10^6 \left[\left(\frac{\sqrt{\overline{p'_s}^2}}{q_\infty} \right) 100 \right]^{-0.25}$$

6.0 CONCLUDING REMARKS

Transition and fluctuating pressure data were acquired on a standard body (AEDC Transition Cone), using the same instrumentation and technique over a wide range of Mach and Reynolds numbers in 23 wind tunnels and in flight. The cone was held at near zero incidence and heat transfer. Transition was detected with a traversing pitot-pressure probe in contact with the surface. The pressure fluctuations at the cone surface were measured with microphones set flush in the cone surface.

There was good correlation between end-of-transition Reynolds numbers Re_T obtained in the lower disturbance wind tunnels and those obtained in flight, up to about $M_e = 1.2$. Above $M_e = 1.2$, the correlation deteriorates, with the flight Re_T being 25% to 30% higher than the wind tunnel Re_T at $M_e = 1.6$. For the higher disturbance tunnels, there was very poor correlation between tunnel and flight Re_T. The end-of-transition Reynolds number correlated within ±20% with the surface-fluctuating root-mean-square pressure level, according to the equation

$$Re_T = 3.7 \times 10^6 \left[\left(\frac{\sqrt{\overline{p'_s}^2}}{q_\infty} \right) 100 \right]^{-0.25}$$

Broad peaks in the spectra indicated that Tollmien-Schlichting waves were the probable cause of transition in flight and at least in some of the wind tunnels. The flow disturbance measured beneath the laminar boundary layer on the cone in the lower disturbance tunnels was about twice that measured in flight. In the higher disturbance tunnels, it was approximately an order of magnitude greater than the flight data.

The flight data showed a strong heat-transfer influence on transition, a delayed transition occurring when the boundary layer was cooled, and an earlier transition occurring when the boundary layer was heated.

REFERENCES

1. Potter, J. L.; and Whitfield, J. D.: Preliminary Study of the Effect of Unit Reynolds Number on Transition Sensitive Data. AEDC-TN-57-37 (AD 135338), Sept. 1957.

2. Morkovin, M. V.: Instability, Transition to Turbulence, and Predictability. AGARD-AG-236, July 1978.

3. Treon, S. L.; Steinle, F. W., Jr.; Hagerman, J. R.; Black, J. A.; and Buffington, R. J.: Further Correlation of Data from Investigations of a High-Subsonic-Speed Transport Aircraft Model in Three Major Transonic Wind Tunnels. AIAA Paper 71-291, Albuquerque, N. Mex., Mar. 1971.

4. Mabey, D. G.: Flow Unsteadiness and Model Vibrations in Wind Tunnels at Subsonic and Transonic Speeds. RAE C.P. No. 1155, Bedford, England, Oct. 1970.

5. Credle, O. P.; and Carleton, W. E.: Determination of Transition Reynolds Number in the Transonic Mach Number Range. AEDC-TR-70-218 (AD 875995), Oct. 1970.

6. Dougherty, N. S., Jr.; and Steinle, F. W., Jr.: Transition Reynolds Number Comparisons in Several Major Transonic Tunnels. AIAA Paper 74-627, Bethesda, Md., July 1974.

7. Vaucheret, X.: Acoustic Fluctuations Generated by the Ventilated Walls of a Transonic Wind Tunnel. Paper No. 25, AGARD Fluid Dynamics Panel Symposium on Wind Tunnel Design and Testing Techniques, AGARD CP-174, London, England, Oct. 6-8, 1975 (also ONERA Chatillon TP No. 1324, 1974).

8. Ross, R.; and Rohne, P. B.: The Character of Flow Unsteadiness and Its Influence on Steady-State Transonic Wind Tunnel Measurements. Paper No. 45, AGARD Fluid Dynamics Panel Symposium on Wind Tunnel Design and Testing Techniques, AGARD CP-174, London, England, Oct. 6-8, 1975 (also MLR Amsterdam TR 74128 U, Aug. 1973).

9. Mabey, D. B.: Boundary-Layer Transition Measurements on the AEDC 10° Cone in Three RAE Wind Tunnels and Their Implications. British ARC R&M 3821, RAE-TR-76077, June 1976.

10. Jordan, R.: Tests with the AEDC 10-Deg Transition Cone in the 9 X 8-Foot Transonic Tunnel. ARA, Ltd. Model Test Note M.32, Apr. 1973.

11. Dougherty, N. S., Jr.: Influence of Wind Tunnel Noise on the Location of Boundary-Layer Transition on a Slender Cone at Mach Numbers from 0.2 to 5.5. AEDC-TR-78-44, 1980.

12. Fisher, David F.; and Dougherty, N. Sam, Jr.: In-Flight Transition Measurements on a 10° Cone at Mach Numbers From 0.5 to 2.0. NASA TP-1971, 1982.

13. Dougherty, N. Sam, Jr.; and Fisher, David F.: Boundary-Layer Transition Correlation on a Slender Cone in Wind Tunnels and Flight for Indications of Flow Quality. AEDC-TR-81-26, Feb. 1982.

14. Dougherty, N. S., Jr.; and Fisher, D. F.: Boundary-Layer Transition on a 10-Degree Cone Wind Tunnel/Flight Data Correlation. AIAA Paper 80-0154, Jan. 1980.

15. Harvey, W. D.: Some Anomalies between Wind Tunnel and Flight Transition Results. AIAA Paper 81-1225, Palo Alto, Calif., June 1981.

16. Herrington, Russel M.; Shoemacher, Paul E.; Bartlett, Eugene P.; and Dunlap, Everett W.: Flight Test Engineering Handbook. AF Tech. Rept. No. 6273, Air Force Flight Test Center, Edwards AFB, Edwards, Calif., June 1964.

17. Larson, Terry J.; and Ehernberger, L. J.: Techniques Used for Determination of Static Source Position Error of a High Altitude Supersonic Airplane. NASA TM X-3152, 1975.

18. Webb, Lannie D.: Characteristics and Use of X-15 Air-Data Sensors. NASA TN D-4597, 1968.

19. Mack, Leslie M.: Boundary-Layer Stability Theory. NASA CR-131501, 1969

20. Reshotko, E.: Drag Reduction by Cooling in Hydrogen Fueled Aircraft. J. Aircraft, vol. 16, Sept. 1979, pp. 584-590.

21. Beckwith, Ivan E.; and Bertram, Mitchel H.: A Survey of NASA Langley Studies on High-Speed Transition and the Quiet Tunnel. NASA TM X-1566, 1972.

22. Potter, J. Leith; and Whitfield, Jack D.: Effect of Unit Reynolds Number, Nose Bluntness, and Roughness on Boundary Layer Transition. AEDC TR-60-5, Arnold Eng. Dev. Center, Mar. 1960.

23. Lowson, M. V.: Prediction of Boundary-Layer Pressure Fluctuations. AFFDL-TR-67-167, Apr. 1968.

TABLE 1. SUMMARY OF WIND TUNNEL CHARACTERISTICS

Group	Tunnel	Mach number range	Unit Reynolds number range $\times 10^6$ per m (per ft)	Predominant disturbances	Resonant Mach number	$(\sqrt{\overline{p_n'^2}}/q_\infty)_{max}$, percent
1	Slotted wall					
	NASA/Langley 8 TPT	0.25-1.20	6.6-9.8 (2.0-3.0)	Low frequency	0.80	2.20
	NASA/Langley 16 TT	0.20-1.30	4.3-12.8 (1.3-3.9)	Low frequency	0.82	3.60
	NASA/Langley 16 TDT (Freon)[a]	0.30-1.15	4.9-12.1 (1.5-3.7)	Low frequency	0.85	1.40
	NSRDC 7 × 10 T	0.20-1.13	4.9-13.1 (1.5-4.0)	Low frequency	0.75	1.26
	NLR 0.55 × 5.28 HST[b]	0.15-1.30	4.9-45.9 (1.5-14.0)	Compressor	0.80	1.01
	RAE Farnborough 8 × 6[c]	0.20-1.19	1.3-8.2 (0.4-2.5)	Compressor	0.60	1.90
	Solid wall –					
	NASA/Ames 12 PT	0.20-0.90	6.6-9.8 (2.0-3.0)	Test Section	0.65	1.05
	RAE Bedford 8 × 8 SWT (subsonic mode)	0.20-0.80	0.8-9.8 (0.25-3.0)		None	0.80
2	Perforated wall					
	AEDC Tunnel 4T	0.40-1.30	4.9-16.4 (1.5-5.0)	Edge tones	0.60/1.30	3.75
	ONERA 6 × 6 S-2 Modane	0.25-1.30	6.6-23.6 (2.0-7.2)	Edge tones	0.80	2.77
	ONERA 2.50 × 1.83 S-3 Modane[b]	0.25-1.00	6.6-41.0 (2.0-12.5)	Stilling chamber	0.25	12.70
	AEDC Tunnel 16T	0.20-1.60	3.3-18.4 (1.0-5.6)	Edge tones	0.71	2.68
	Calspan 8 TWT	0.60-0.95	6.6-9.8 (2.0-3.0)	Wall tones	0.85	2.10
	ARA, Ltd. Bedford 9 × 8[d]	0.21-1.40	4.9-14.4 (1.5-4.4)	Wall tones	0.68	2.65
	Corrugated-slot wall –					
	NASA/Ames 11 TWT	0.40-1.20	4.9-19.7 (1.5-6.0)	Slot organ pipe	0.75	2.00
	NASA/Ames 14 TWT	0.40-1.05	8.5-13.1 (2.6-4.0)	Slot organ pipe	0.95	2.05
3	Convergent/divergent nozzle –					
	RAE Bedford 8 × 8 SWT[e]	1.40-2.40	2.0-13.1 (0.6-4.0)	Wall boundary layer	None	0.45
	NASA/Langley 4 SPT	1.61-2.01	3.3-16.4 (1.0-5.0)	Wall boundary layer	None	0.12
	AEDC Tunnel 16S	1.07-2.20	3.0-7.2 (0.9-2.2)	Wall boundary layer	None	0.50
	AEDC VKF Tunnel A	1.51-5.50	7.5-22.3 (2.3-6.8)	Wall boundary layer	None	-----
	RAE Bedford 3 × 4 HSST	2.50-4.50	2.3-30.1 (0.7-9.2)	Wall boundary layer	None	0.20
4	Sliding-block nozzle –					
	NASA/Ames 9 × 7 SWT	1.50-2.50	6.6-14.8 (2.0-4.5)	Wall boundary layer	None	0.18
	NASA/Langley 4 SUPWT (TS No. 1)	1.60-2.86	4.9-16.4 (1.5-5.0)	Wall boundary layer	None	0.14
	NASA/Langley 4 SUPWT (TS No. 2)	2.86-4.60	4.9-21.3 (1.5-6.5)	Wall boundary layer	None	0.24

[a]Tests performed using both Freon and air as tunnel working fluid

[b]Only noise data, no transition data

[c]Results affected by model surface imperfections during this test

[d]Transition data at Mach numbers from 0.2 to 0.6 only

[e]Data acquired in Mach number range from 0.2 to 0.8 also

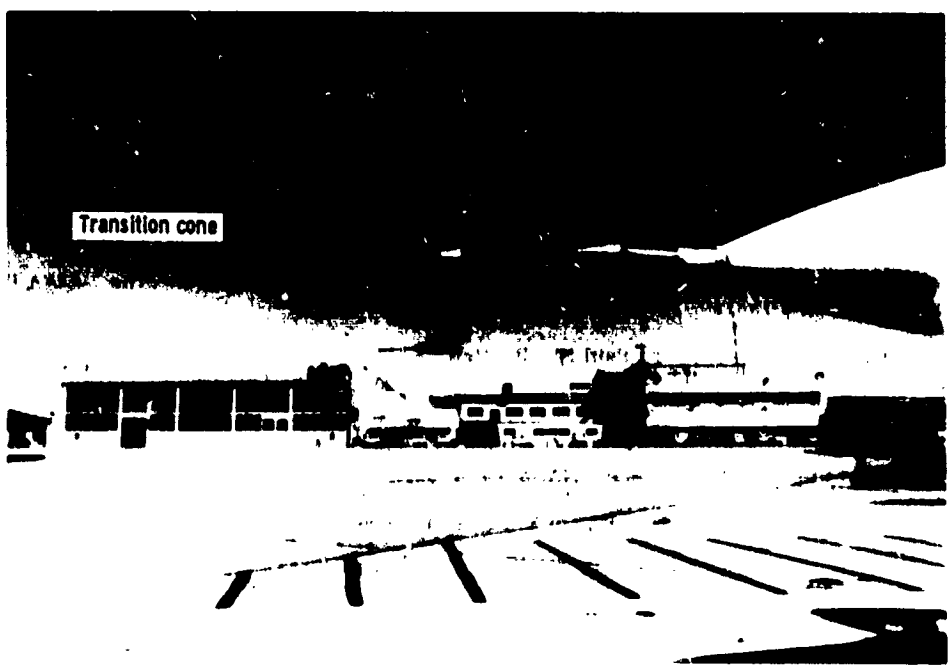

(a) Mounted on aircraft.

Figure 1. Transition cone and instrumentation.

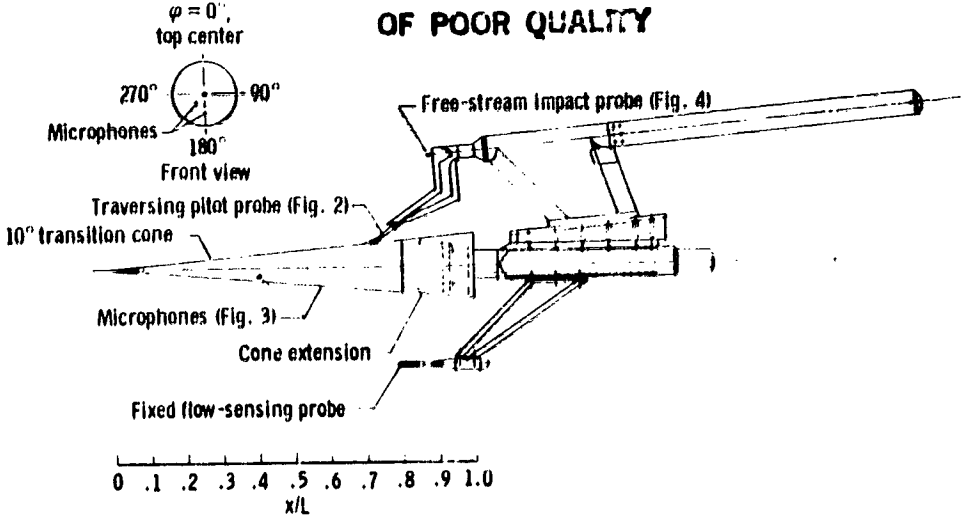

(b) Location of instrumentation.

(c) Installed in AEDC VKF Tunnel A.

Figure 1. Concluded.

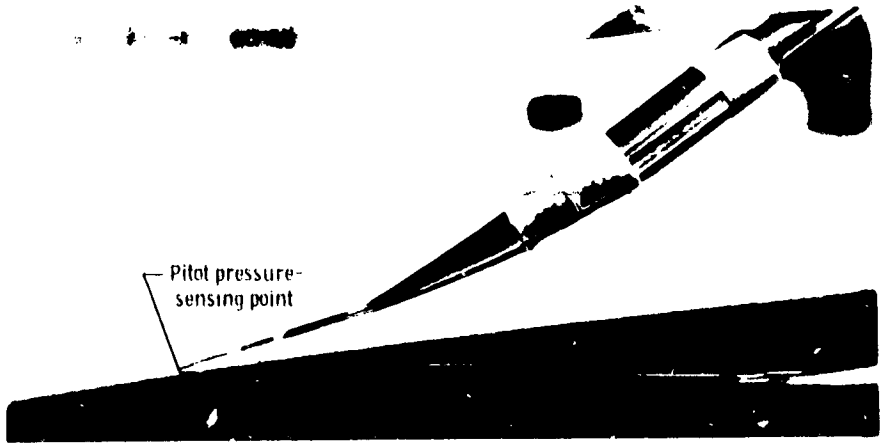

(a) Photograph.

Figure 2. Pitot pressure probe.

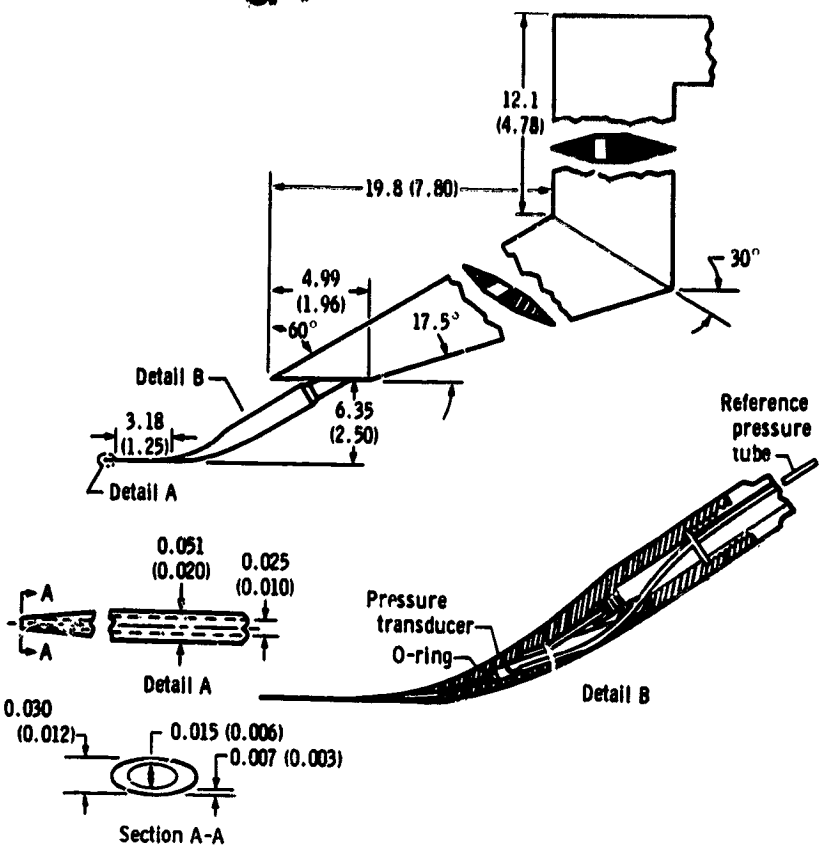

(b) Details. Dimensions are in centimeters (inches).

Figure 2. Concluded.

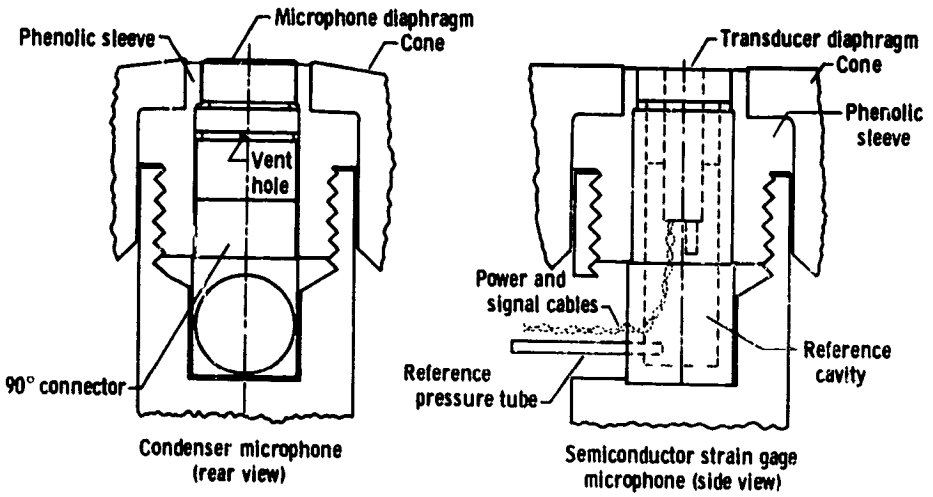

Figure 3. Flush-mounted microphone installations.

Figure 4. Probe for measuring fluctuating free-stream impact pressure.

Figure 5. Transition cone mounted in front of test-bed aircraft.

Figure 6. Transition cone being heated at end of runway before flight.

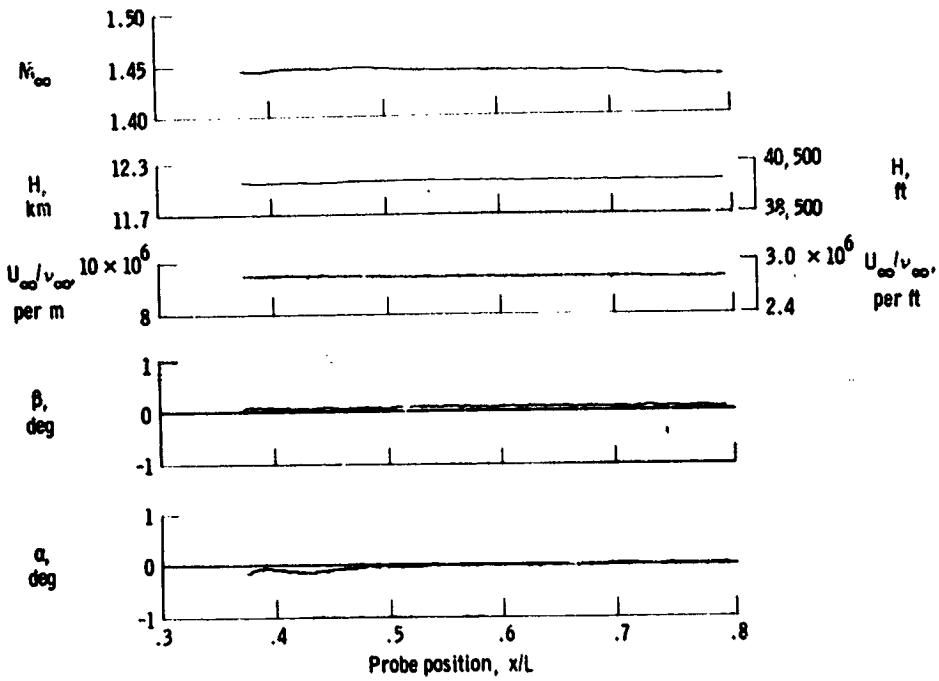

Figure 7. History of cone free-stream conditions during a typical pitot-probe traverse.

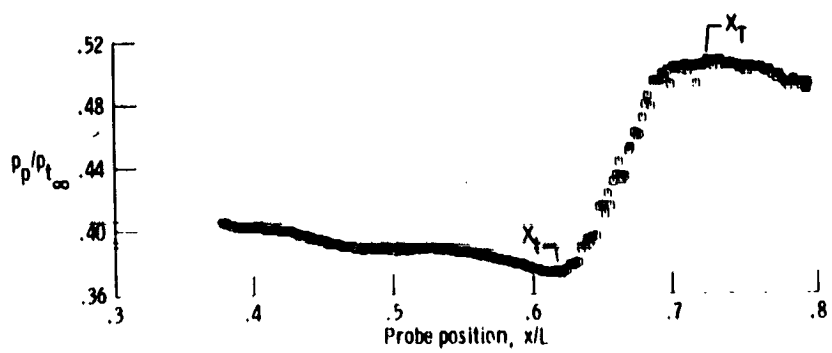

Figure 8. Typical pitot probe pressures as a function of probe location. $M_\infty = 1.44$.

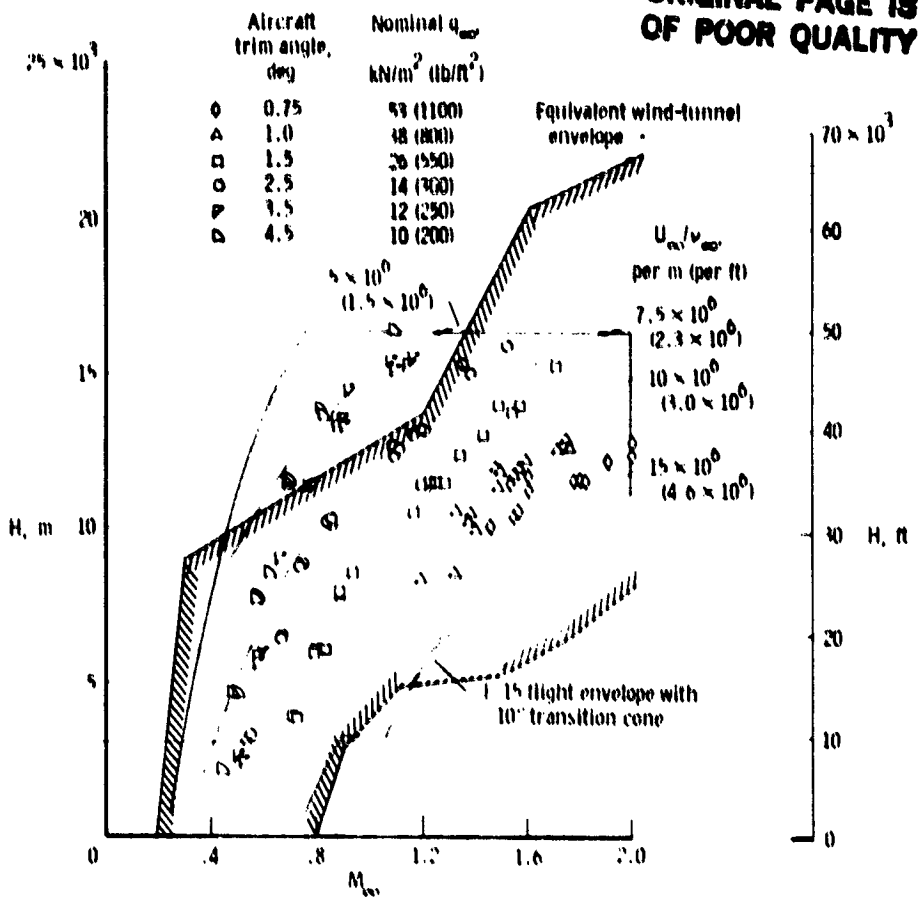

Figure 9. Transition cone flight test matrix and equivalent wind tunnel envelope.

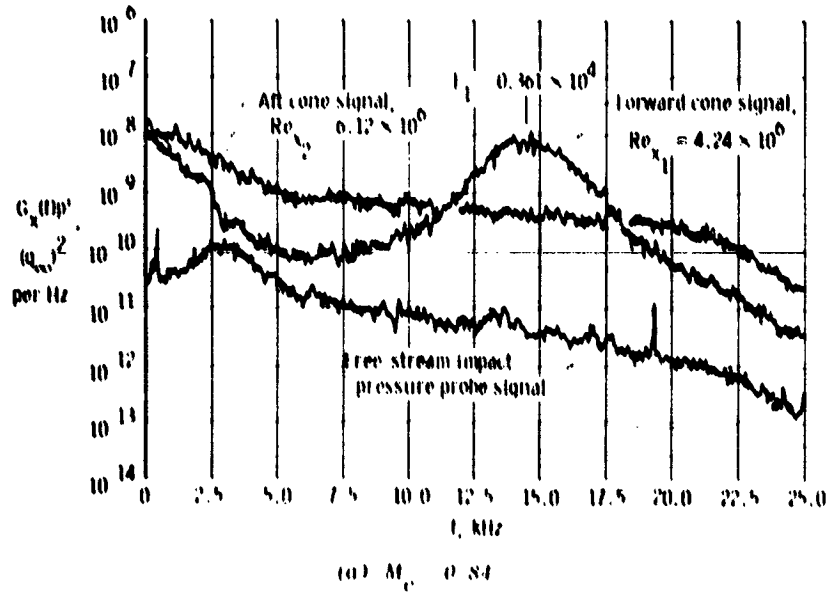

(a) M_∞ 0.84

Figure 10. Microphone power spectral density distribution

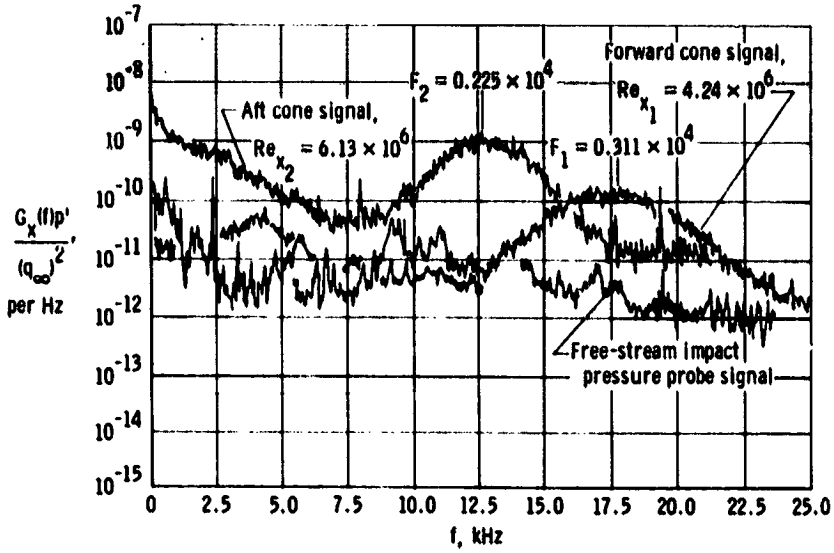

(b) $M_e = 1.31$.

Figure 10. Concluded.

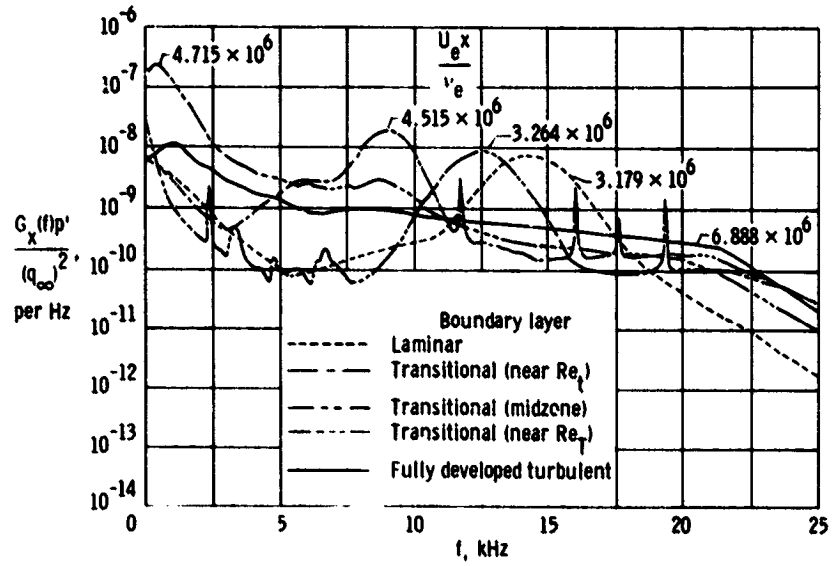

(a) $M_e \approx 0.8$.

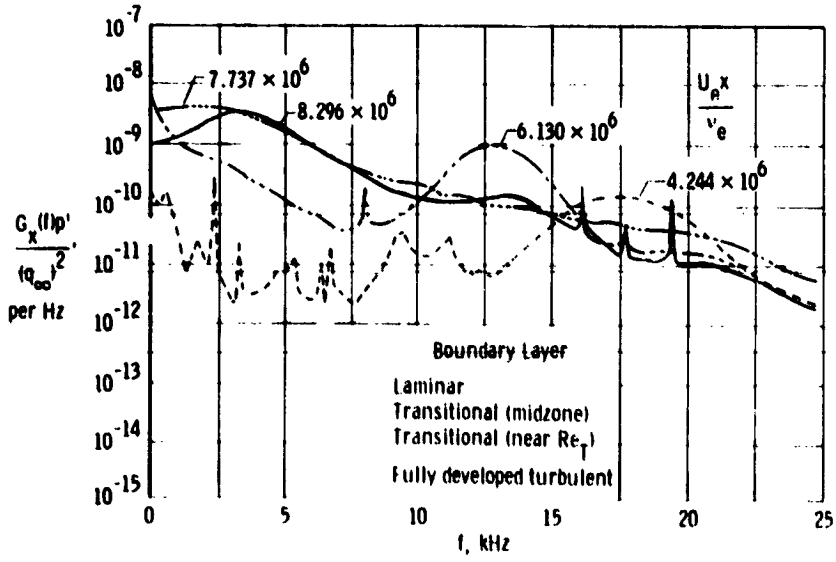

(b) $M_e \approx 1.35$.

Figure 11. Effect of Reynolds number on power spectral density distribution (spectra are smoothed).

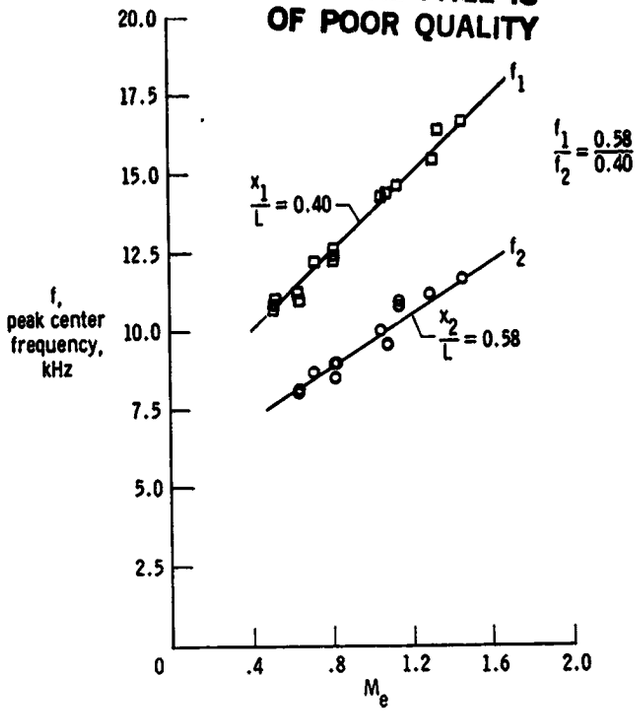

Figure 12. Variation of laminar or transitional spectral peak frequency with local Mach number; $q_\infty \approx 14.4\ kN/m^2$ (300 lb/ft^2).

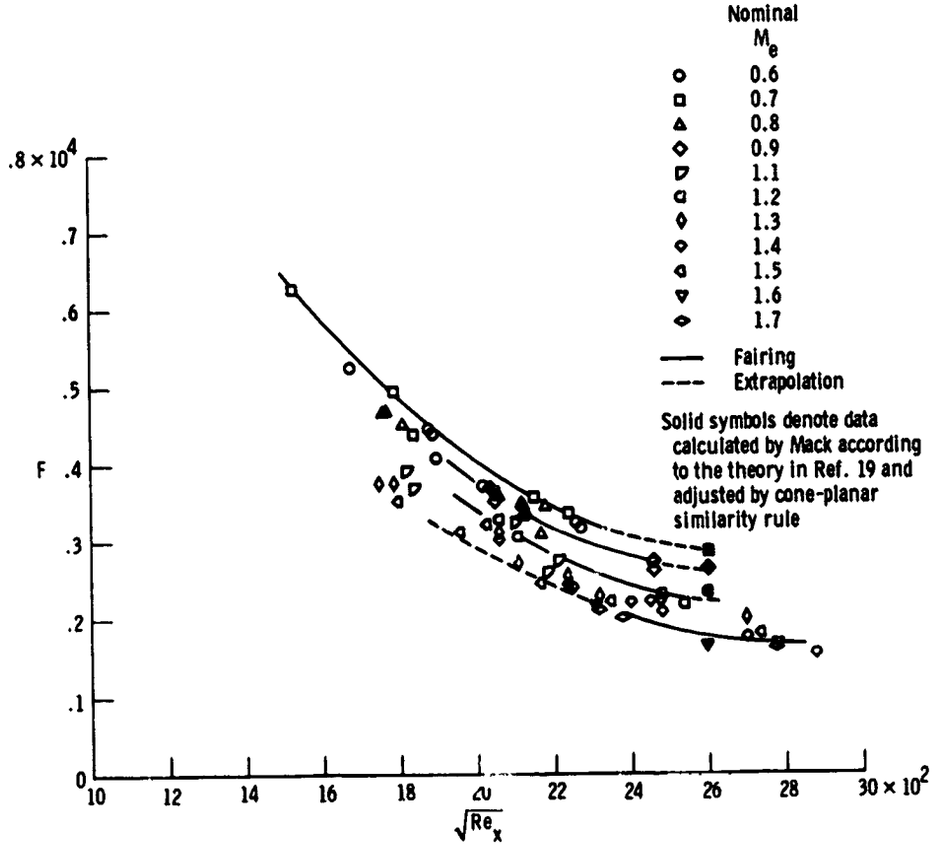

Figure 13. Variation of nondimensional frequency with Re_x.

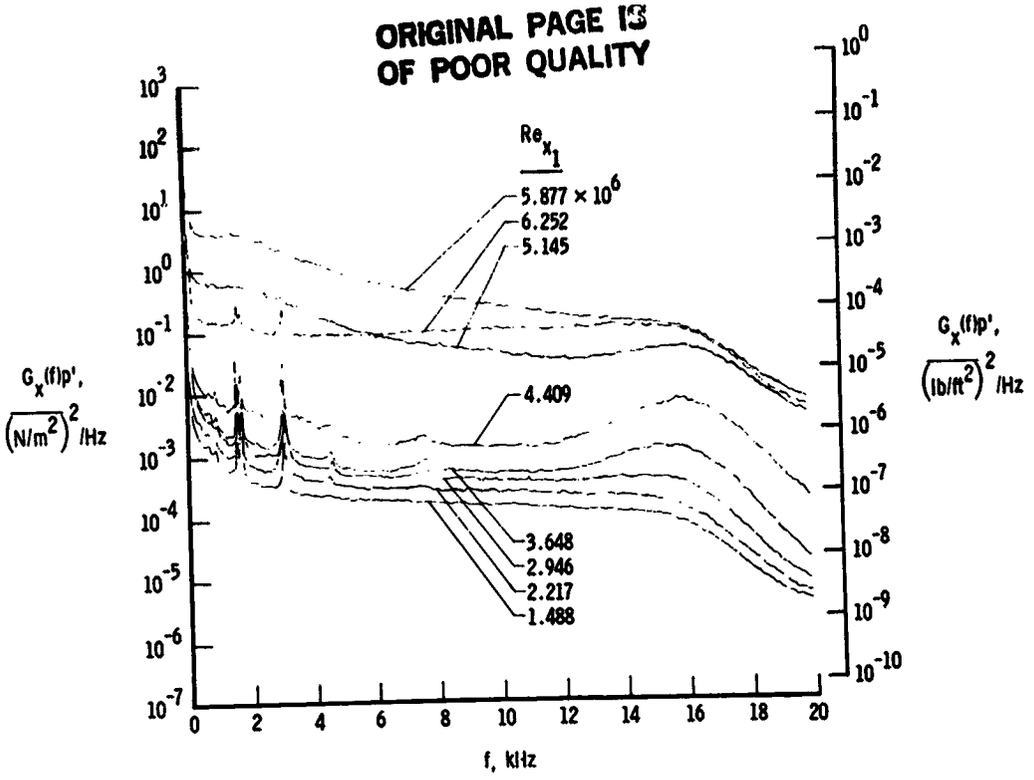

(a) Forward microphone.

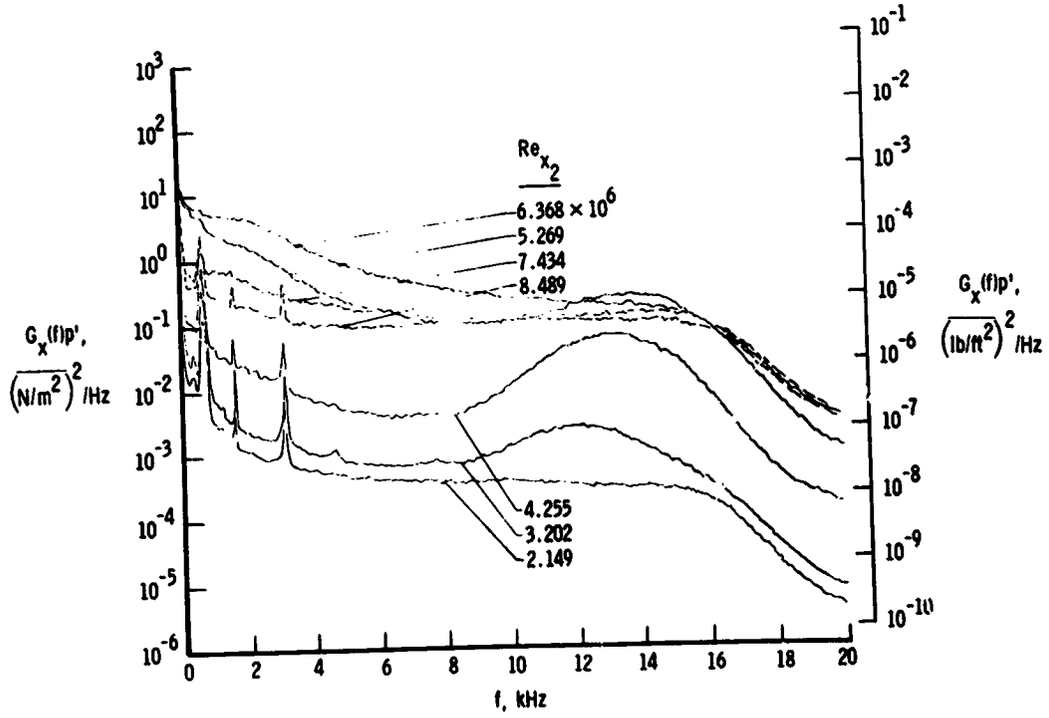

(b) Aft microphone.

Figure 14. Cone microphone spectra in the Langley 4 SPT at $M_\infty = 1.61$ ($M_\infty = 1.57$).

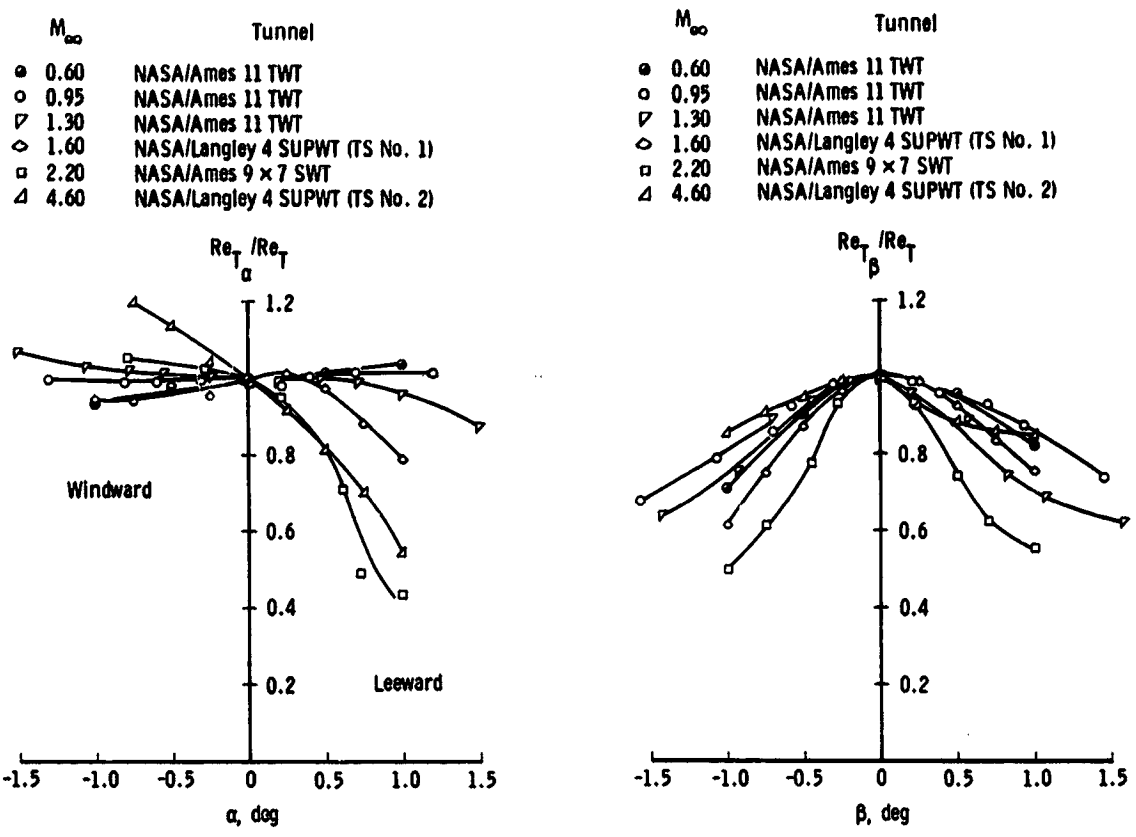

(a) Angle-of-attack influence. Re_{T_α} normalized by Re_T at $\alpha = 0°$; all data shown at $\beta = 0°$.

(b) Angle-of-sideslip influence. Re_{T_β} normalized by Re_T at $\beta = 0°$; all data shown at $\alpha = 0°$.

Figure 15. Summary of the effect of model incidence angle (α and β) on transition.

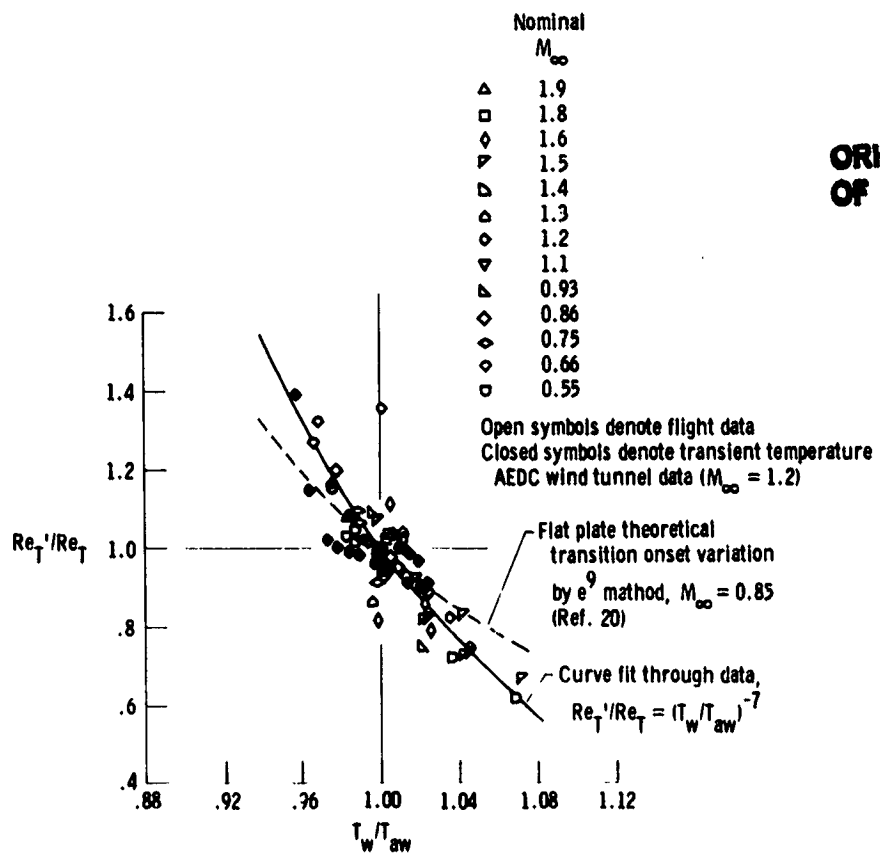

Figure 16. Variation in flight-determined transition Reynolds number with wall temperature and comparison with theoretical and wind-tunnel results.

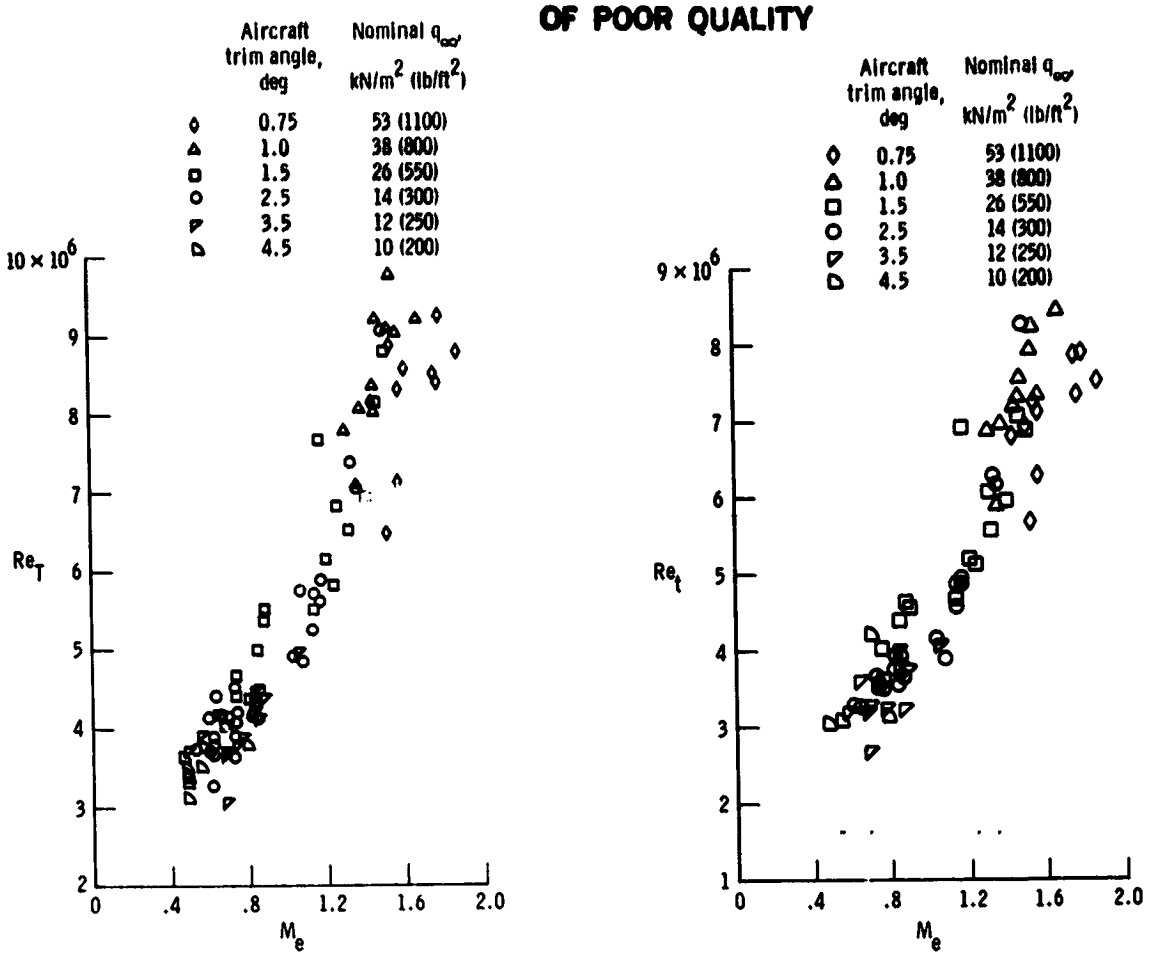

(a) End-of-transition Reynolds number. *(b) Onset-of-transition Reynolds number.*

Figure 17. Transition Reynolds number as a function of Mach number.

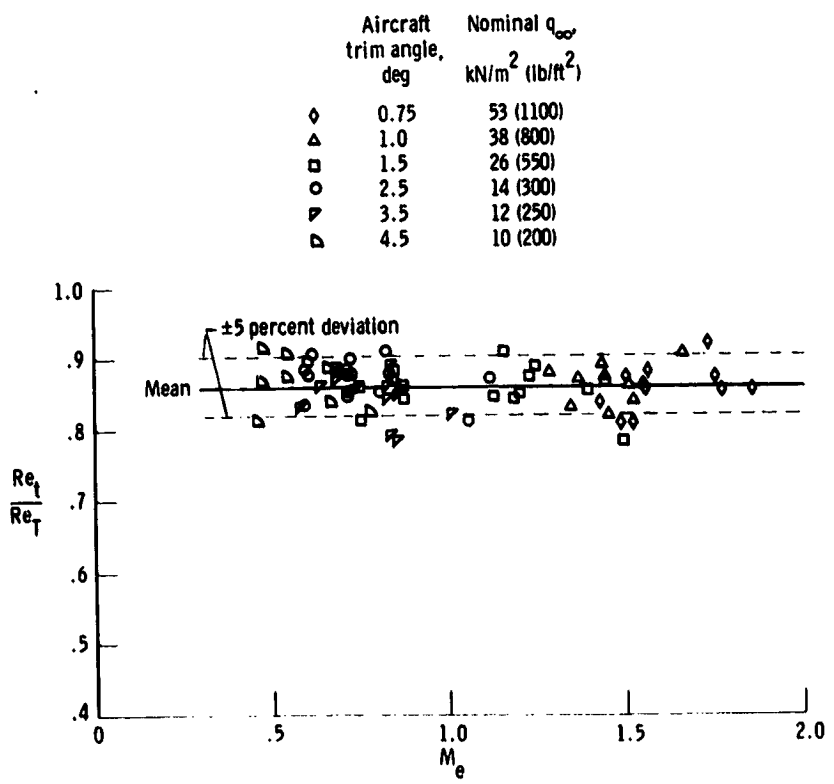

Figure 18. Ratio of onset-of-transition Reynolds number to end-of-transition Reynolds number as a function of Mach number.

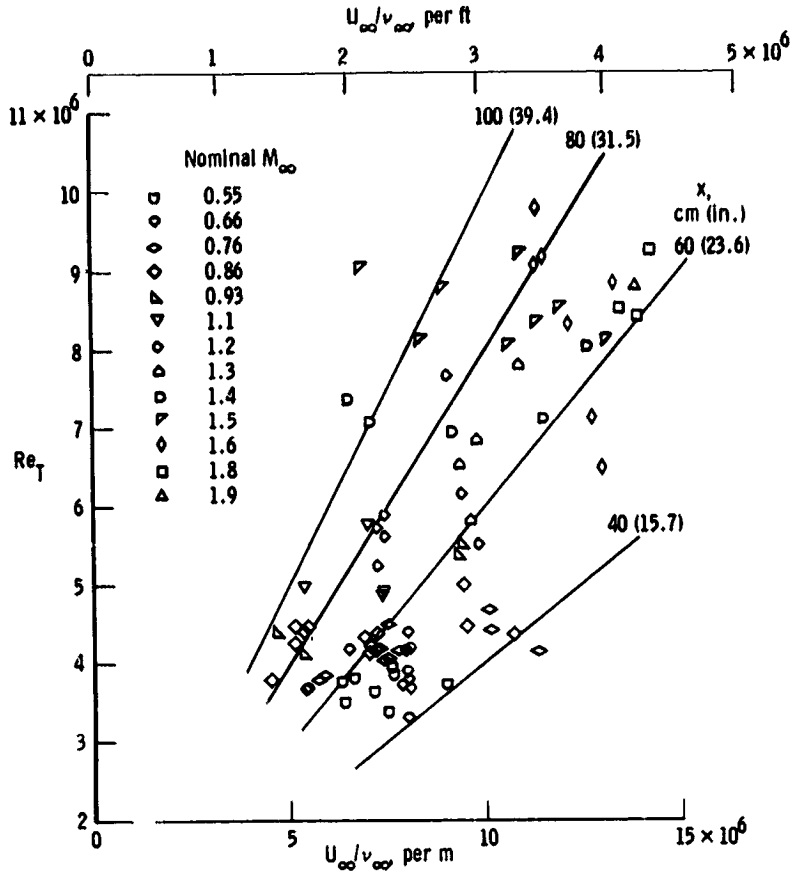

Figure 19. Transition Reynolds number as a function of unit Reynolds number.

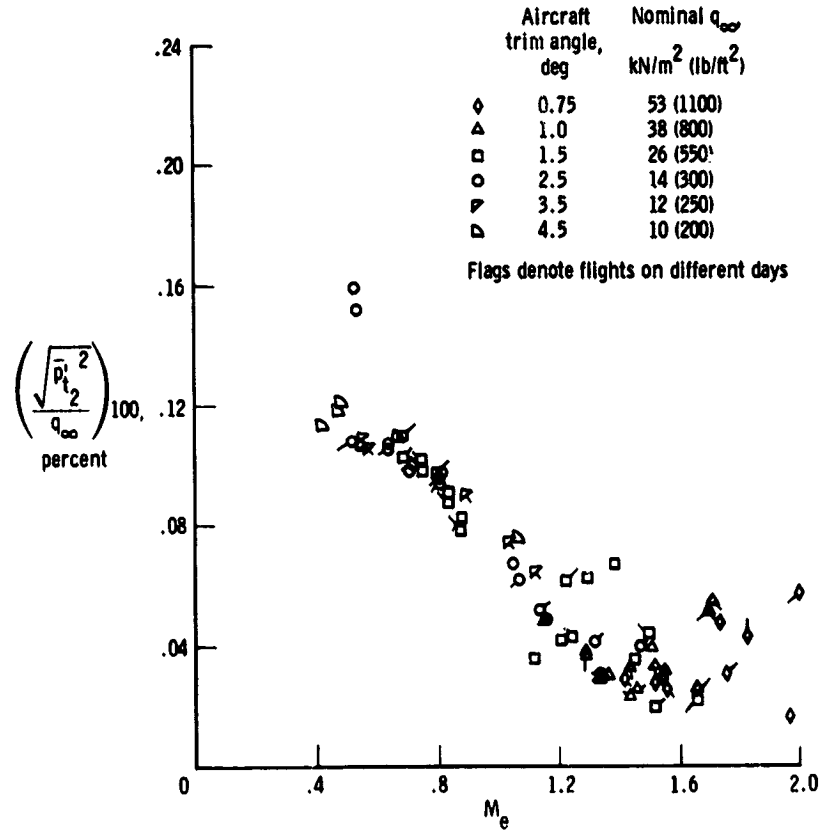

Figure 20. Fluctuating free-stream impact pressure as a function of local Mach number.

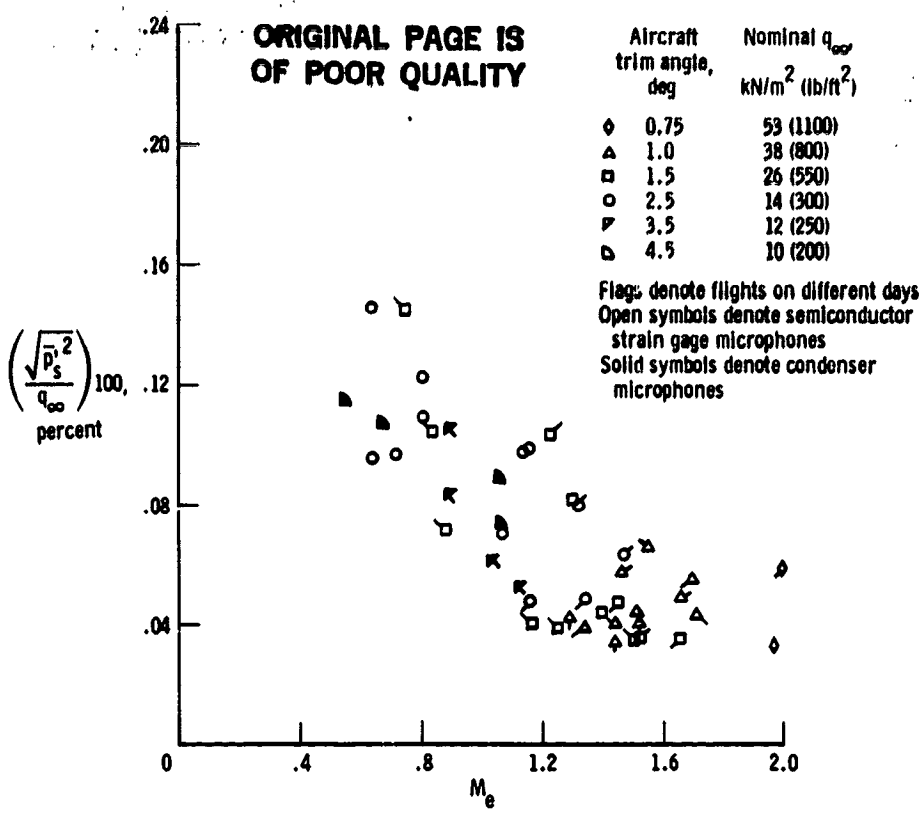

Figure 21. Fluctuating static pressure as a function of local Mach number.

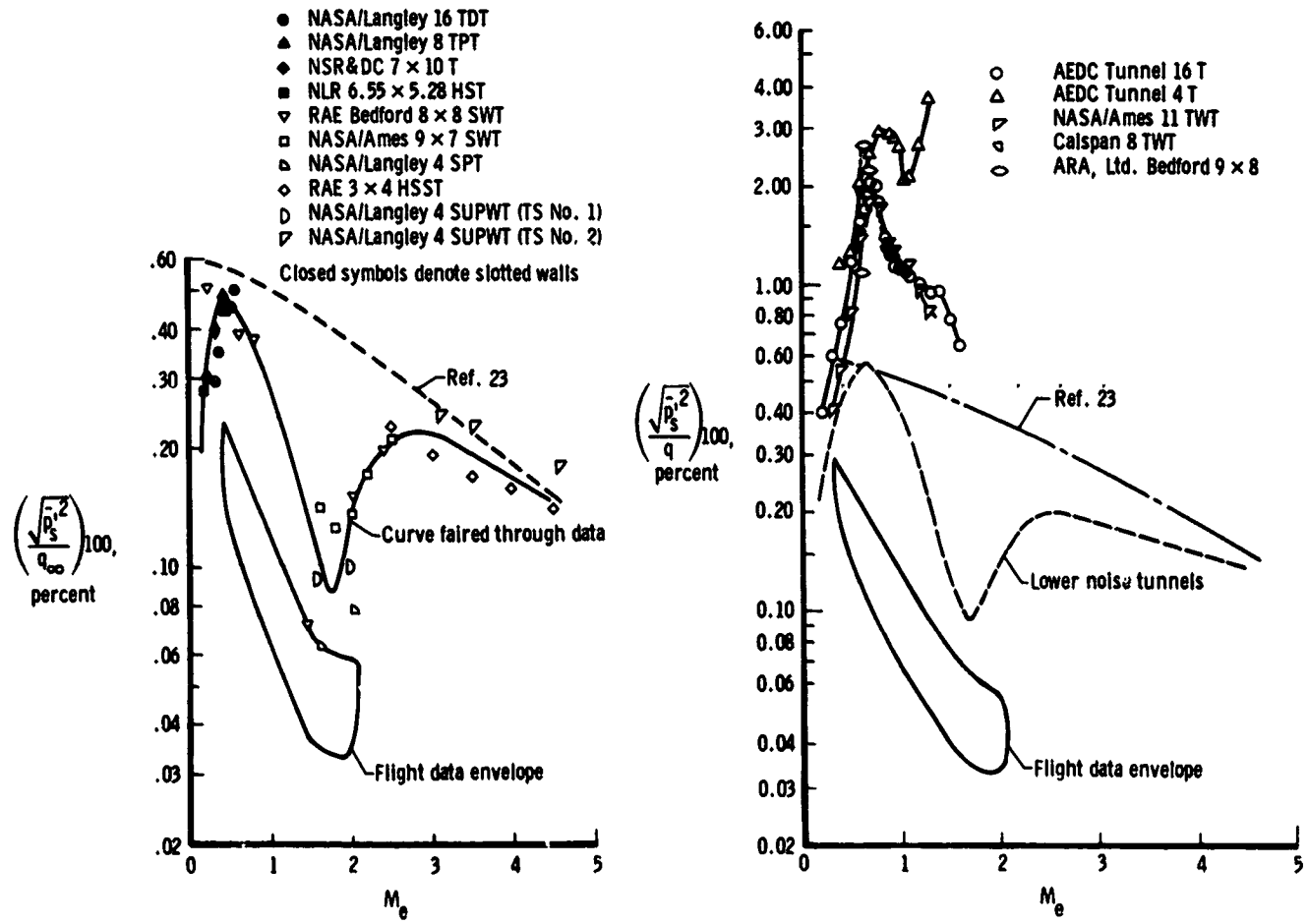

(a) Group 1, 3, and 4 wind tunnels. $U_\infty/\nu_\infty \approx 9.8 \times 10^6\ m^{-1}$ $(3.0 \times 10^6\ ft^{-1})$.

(b) Group 2 wind tunnels. $U_\infty/\nu_\infty \approx 9.8 \times 10^6\ m^{-1}$ $(3.0 \times 10^6\ ft^{-1})$.

Figure 22. Comparison of pressure fluctuation levels measured in wind tunnels and disturbances in flight.

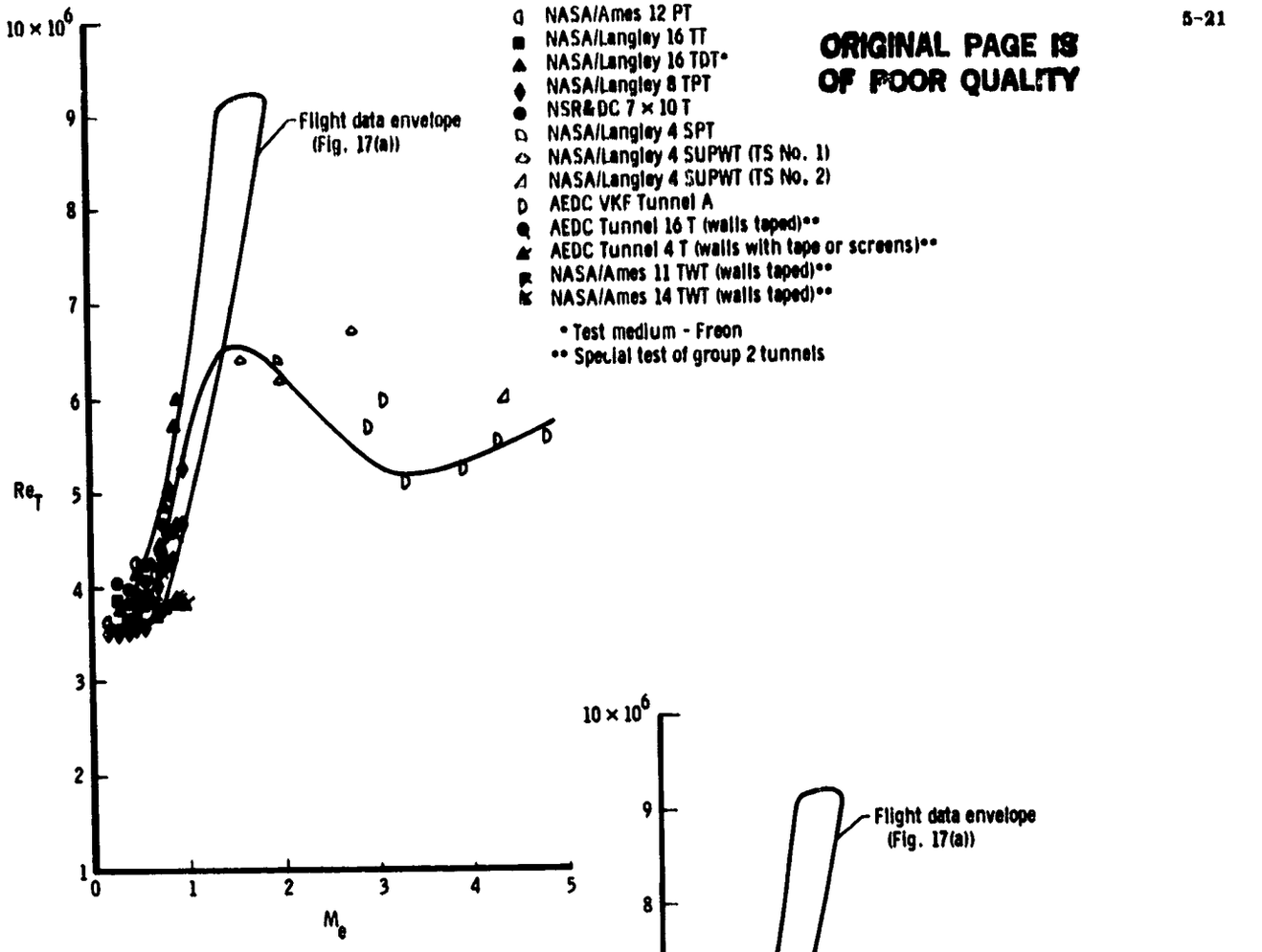

(a) $U_\infty/\nu_\infty = 6.6 \times 10^6\ m^{-1}\ (2.0 \times 10^6\ ft^{-1})$.

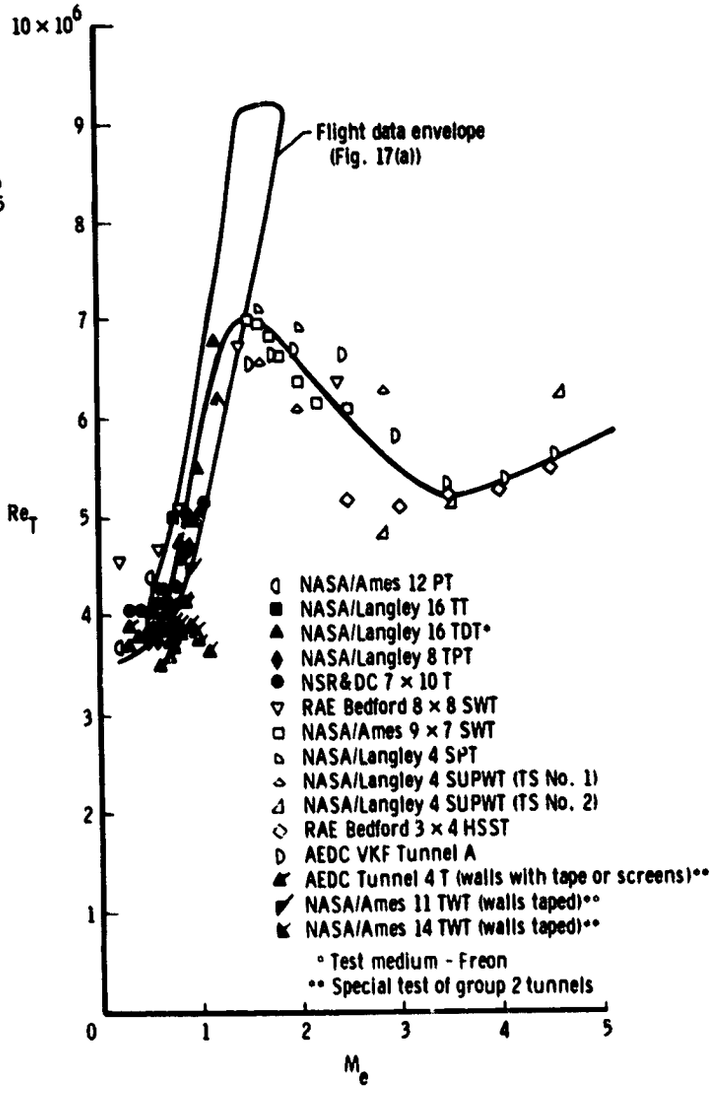

(b) $U_\infty/\nu_\infty = 9.8 \times 10^6\ m^{-1}\ (3.0 \times 10^6\ ft^{-1})$.

Figure 23. End-of-transition Reynolds number obtained in Group 1, 3, and 4 wind tunnels.

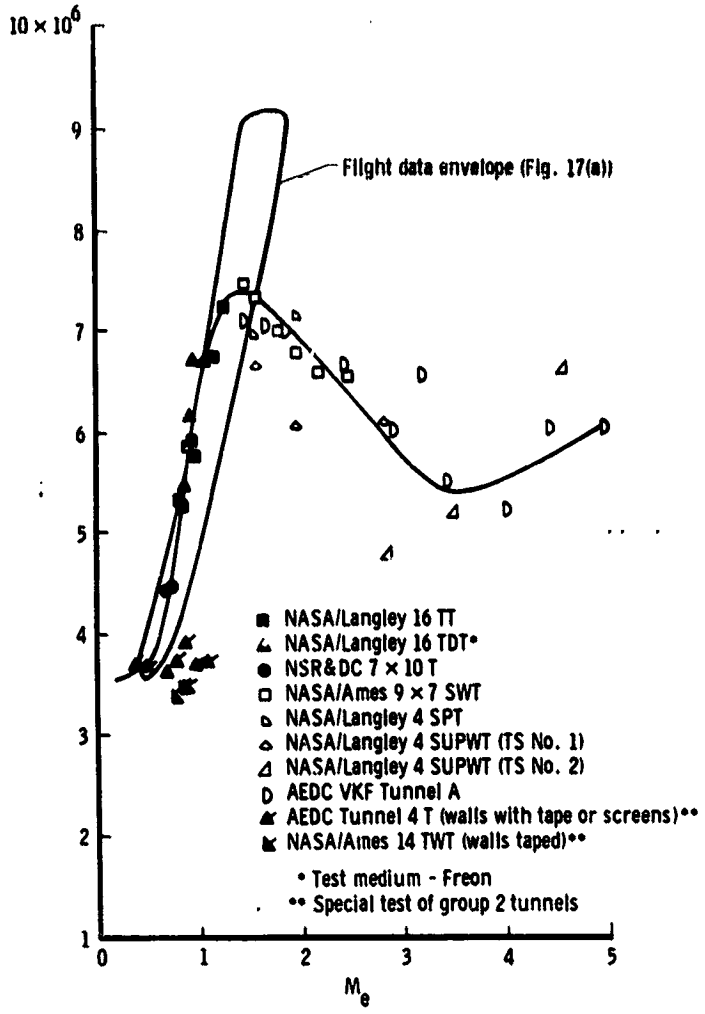

(c) $U_\infty/\nu_\infty = 13.1 \times 10^6\ m^{-1}\ (4.0 \times 10^6\ ft^{-1})$.

Figure 23. Concluded.

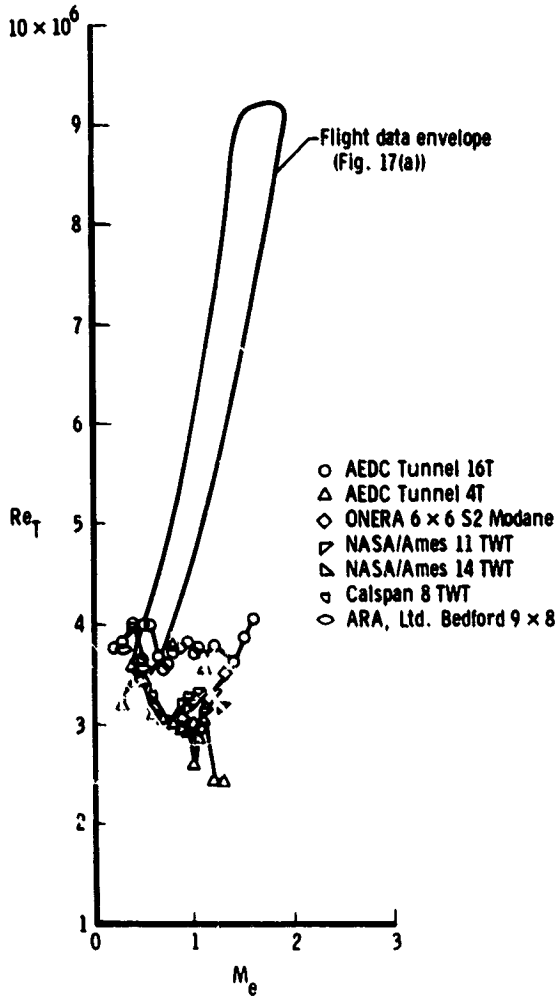

(a) $U_\infty/\nu_\infty = 6.6 \times 10^6\ m^{-1}\ (2.0 \times 10^6\ ft^{-1})$.

Figure 24. End-of-transition obtained in group 2 wind tunnels.

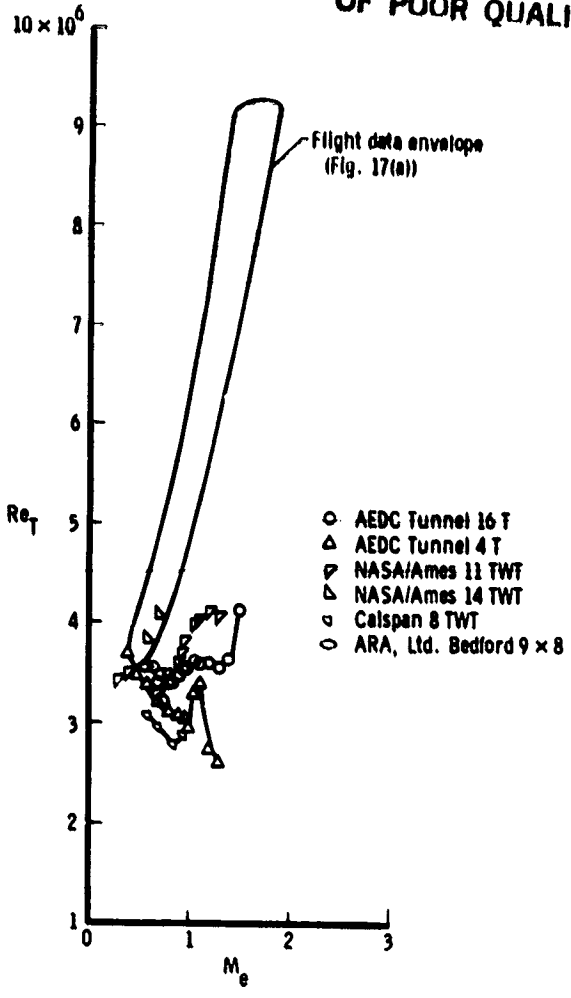

(b) $U_\infty/\nu_\infty = 9.8 \times 10^6\ m^{-1}\ (3.0 \times 10^6\ ft^{-1})$.

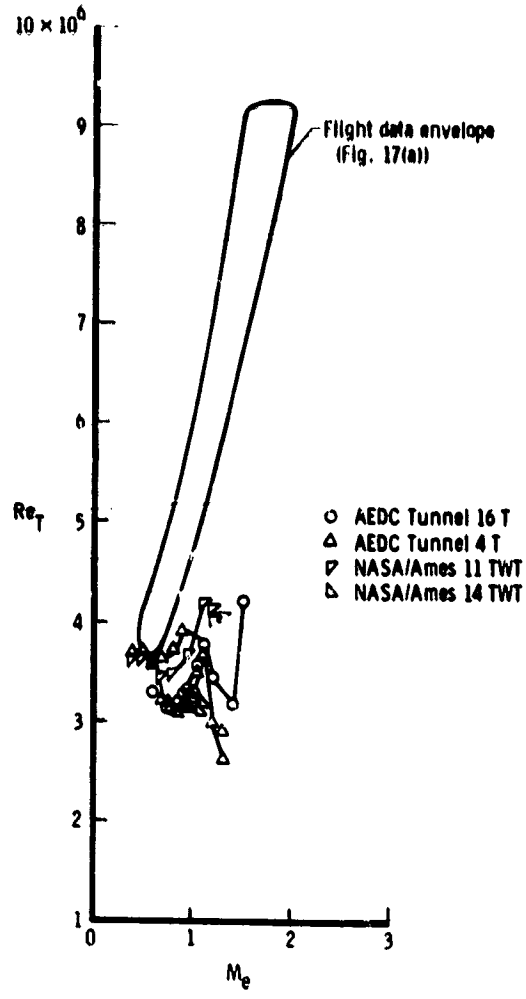

(c) $U_\infty/\nu_\infty = 13.1 \times 10^6\ m^{-1}\ (4.0 \times 10^6\ ft^{-1})$.

Figure 24. Concluded.

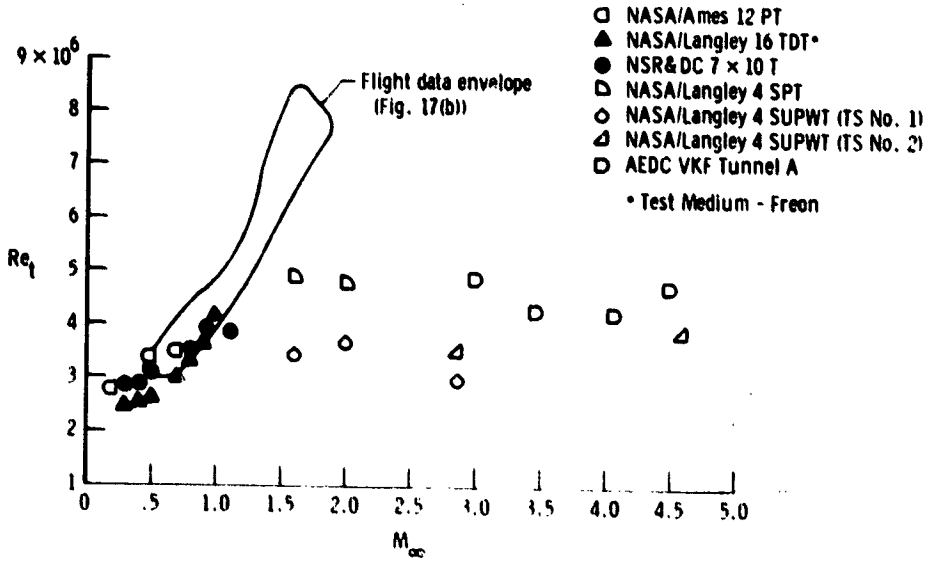

(a) $U_\infty/\nu_\infty = 6.6 \times 10^6\ m^{-1}\ (2.0 \times 10^6\ ft^{-1})$.

Figure 25. Onset-of-transition Reynolds number from lower disturbance wind tunnels and comparison with flight data.

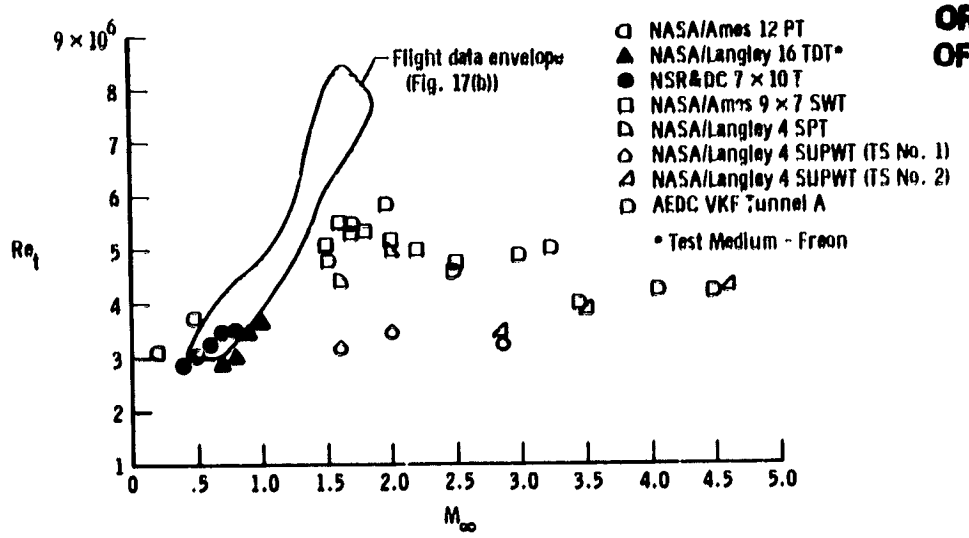

(b) $U_\infty/\nu_\infty = 9.8 \times 10^6\ m^{-1}\ (3.0 \times 10^6\ ft^{-1})$.

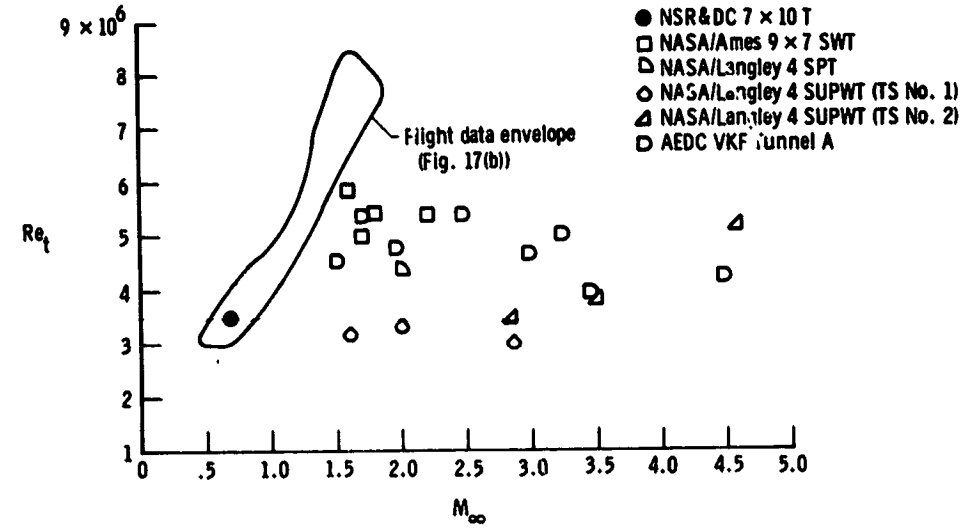

(c) $U_\infty/\nu_\infty = 13.1 \times 10^6\ m^{-1}\ (4.0 \times 10^6\ ft^{-1})$.

Figure 25. Concluded.

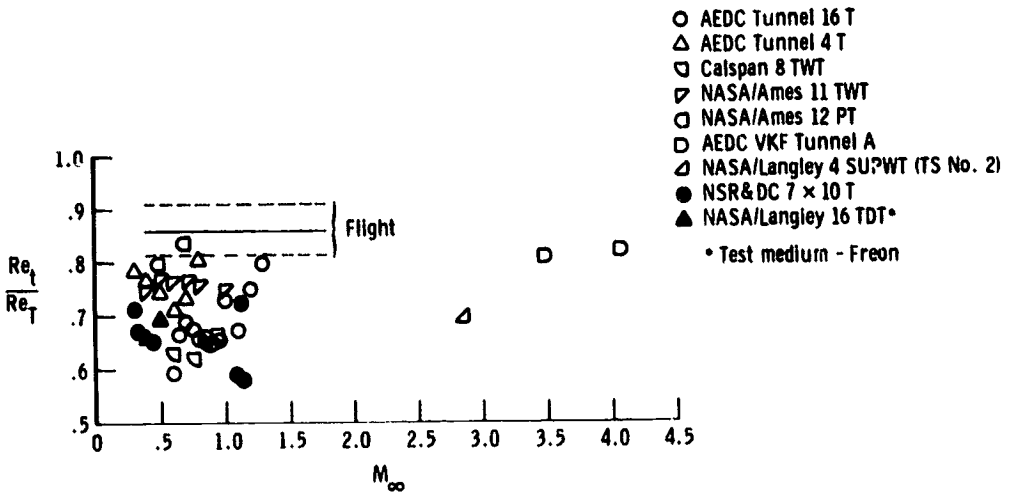

(a) $U_\infty/\nu_\infty = 6.6 \times 10^6\ m^{-1}\ (2.0 \times 10^6\ ft^{-1})$.

Figure 26. Ratio of onset- to end-of-transition Reynolds number from wind tunnels and comparison with flight data.

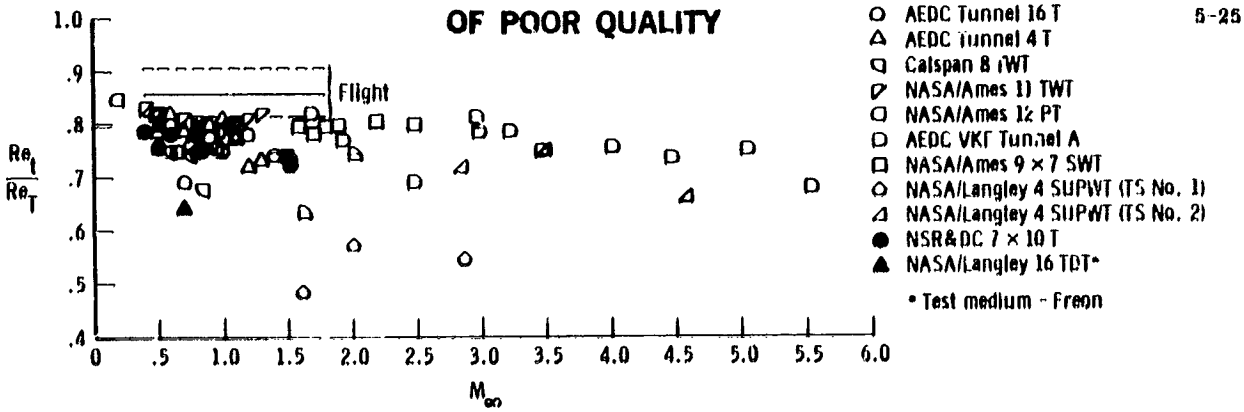

(b) $U_\infty/\nu_\infty = 9.8 \times 10^6\ m^{-1}\ (3.0 \times 10^6\ ft^{-1})$.

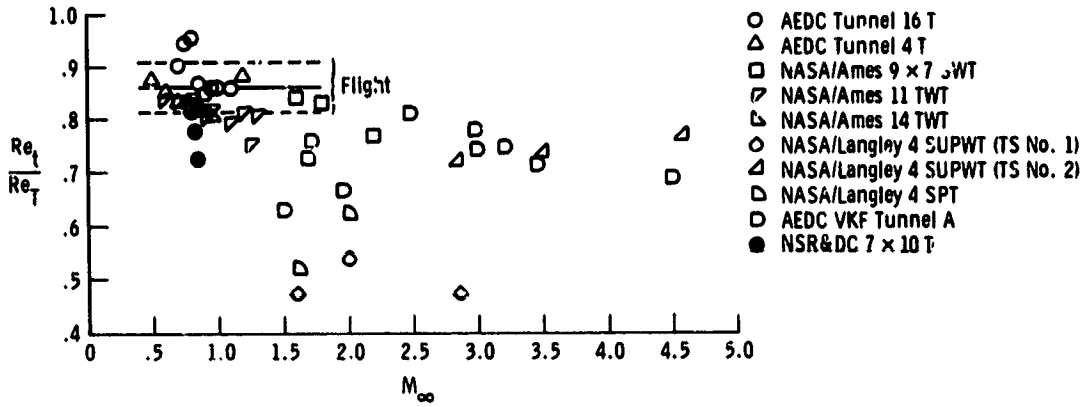

(c) $U_\infty/\nu_\infty = 13.1 \times 10^6\ m^{-1}\ (4.0 \times 10^6\ ft^{-1})$.

Figure 26. Concluded.

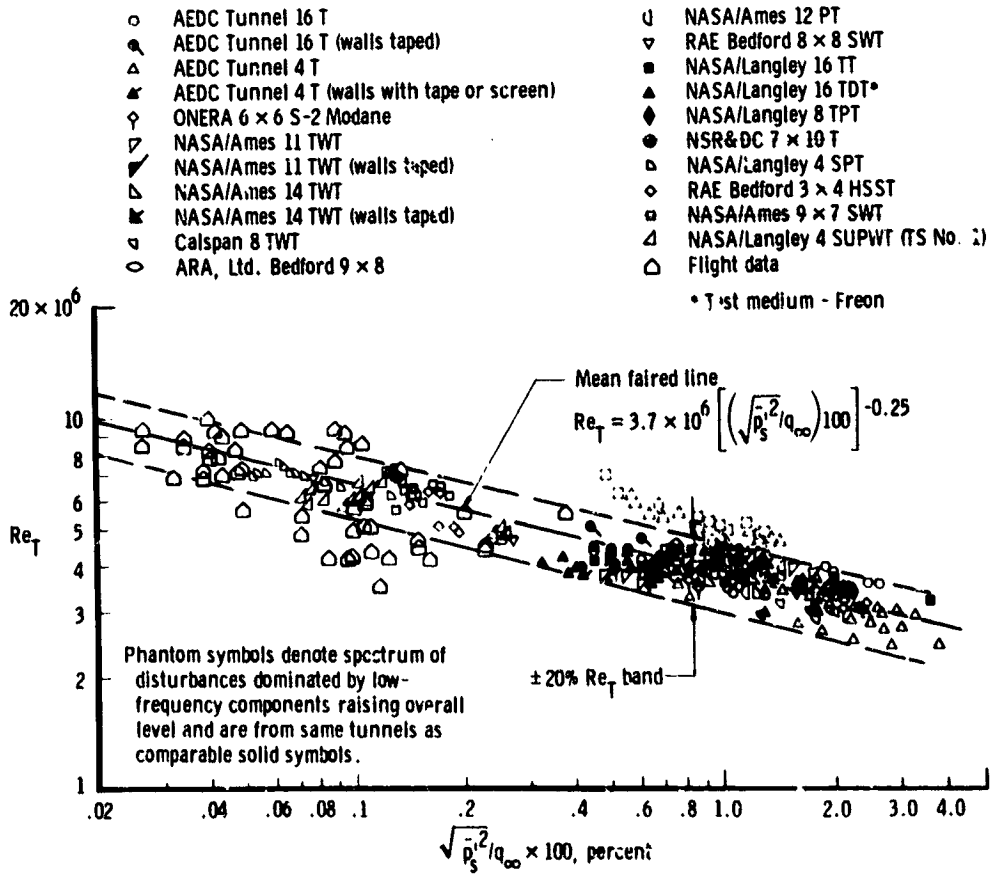

Figure 27. Correlation between Re_T and cone surface disturbance measurements.